All-optical dynamical Casimir effect in a three-dimensional terahertz photonic band gap

David Hagenmüller*

IPCMS (UMR 7504) and ISIS (UMR 7006), Université de Strasbourg and CNRS, Strasbourg, France

(Received 21 January 2016; revised manuscript received 26 May 2016; published 20 June 2016)

We identify an architecture for the observation of all-optical dynamical Casimir effect in realistic experimental conditions. We suggest that by integrating quantum wells in a three-dimensional (3D) photonic band-gap material made out of large-scale ($\sim$200-μm) germanium logs, it is possible to achieve ultrastrong light-matter coupling at terahertz frequencies for the cyclotron transition of a two-dimensional electron gas interacting with long-lived optical modes, in which vacuum Rabi splitting is comparable to the Landau level spacing. When a short, intense electromagnetic transient of duration $\sim$250 fs and carrying a peak magnetic field $\sim$5 T is applied to the structure, the cyclotron transition can be suddenly tuned on resonance with a desired photon mode, switching on the light-matter interaction and leading to a Casimir radiation emitted parallel to the quantum well plane. The radiation spectrum consists of sharp peaks with frequencies coinciding with engineered optical modes within the 3D photonic band gap, and its characteristics are extremely robust to the nonradiative damping which can be large in our system. Furthermore, the absence of continuum with associated low-energy excitations for both electromagnetic and electronic quantum states can prevent the rapid absorption of the photon flux which is likely to occur in other proposals for all-optical dynamical Casimir effect.

DOI: 10.1103/PhysRevB.93.235309

I. INTRODUCTION

The study of light-matter coupling in confined geometries has been actively investigated in many different fields over the past decades. From large-dipole atomic systems interacting with photons in superconducting cavities [1,2], quantum-confined excitations in semiconductor microcavities [3,4], to superconducting qubits coupled to microwave transmission line resonators [5,6], the strong mutual interaction provides opportunities for studying quantum effects at mesoscopic scales. In the strong coupling regime, an electronic resonance is dressed by many photon absorption and reemission cycles, before the system loses its coherence due its interaction with the surrounding environment. The light-matter coupling, quantified by the vacuum Rabi frequency (VRF) Ω, leads to quasibosonic, mixed exciton-photon stationary states called polaritons, separated by an energy termed vacuum Rabi splitting [1].

Quantum-confined excitations in metallic and semiconductor-based cavities cover a wide frequency range, from the far to near infrared, and provide remarkable collective phenomena such as optical parametric oscillations, polariton superfluidity, and Bose-Einstein condensation at high temperature [7,8]. Despite the advent of high-quality samples, condensed-matter systems involve numerous nonradiative decay and decoherence channels, generally leading to much smaller lifetimes than isolated atoms. Moreover, the polariton lifetime in traditional optical cavities is limited by the very short photon decay time ($\tau_{ph} \sim$ 1–10 ps) due to radiative decay into extraneous optical modes that are degenerate with the designed cavity mode.

Extraneous optical modes for spontaneous emission are eliminated using three-dimensional (3D) periodic dielectric structure, known as photonic band-gap (PBG) materials [9–11]. The light localization occurring in PBG materials enables control of the propagation without recourse to the refractive index guiding mechanism used in standard dielectric cavities, and without the high absorption losses occurring in reflecting metallic cavities [12]. When emitters are embedded in a 3D PBG material, quantum coherence is protected by the complete supression of spontaneous emission into extraneous modes [13]. Even without a 3D PBG, two-dimensional (2D) photonic crystals embedded in planar waveguides at submicron scales [14] have provided strong coupling between high-Q photonic modes and quantum emitters integrated in a slab [15–18].

Going down to far-infrared frequencies, PBG materials have been used as efficient substrates for integrated terahertz (THz) sources [19], and provide strong reduction of waveguide losses in the context of THz spectroscopy [20,21] and semiconductor quantum cascade lasers [22,23]. Despite the fact that the excitation decay rates due to nonradiative processes typically increase by several orders of magnitude due to the presence of nearby phonons, a new opportunity arises since the ratio between the VRF and the bare excitations frequency ω increases as well. When this ratio is of order unity ($\Omega/\omega \lesssim 1$) and the polariton splitting is spectrally resolved, the system is in the ultrastrong light-matter coupling regime [24]. This regime has been widely investigated in the context of intersubband excitations in traditional metallic and semiconductor-based microcavities [25–28], as well as more recently using metamaterial resonators [29]. In the ultrastrong coupling regime, both counter-rotating contributions and the so-called $\mathbf{A}^2_{em}$ term affect the polariton spectrum importantly. The energy of the ground state (vacuum) is shifted, and the latter contains a finite number of virtual excitations that can in principle be released as correlated photon pairs when the light-matter coupling is modulated faster than the bare excitations frequency [24,30]. This is an example of the so-called dynamical Casimir effect, originally predicted in the absence of light-matter coupling, when a plane metallic mirror is nonuniformly accelerated through the vacuum, changing its energy or equivalently the local amplitude of the zero-point fluctuations [31]. This modulation

*dhagenmuller@unistra.fr

 ©2016 American Physical Society

gives rise to a dissipative force from the vacuum itself and photon pairs are emitted [32]. Due to the extreme weakness of this force and the emitted radiation, this effect was observed for the first time only recently, in the context of superconducting circuits operating at microwave frequencies [33]. In this case, the effective length of a transmission line is changed by modulating the inductance of a superconducting quantum interference device. In optical cavities, nonlinear properties can be exploited as well: the vacuum energy can be modulated by changing the refractive index of the intracavity medium with a laser pulse [34–36]. Other theoretical proposals have simulated moving cavity mirrors by using a dense electron-hole plasma layer in the cavity [37], or by changing the reflection properties of a composite mirror [38].

In the presence of an ultrastrong light-matter interaction, the idea is to modulate the coupling parameters to change the vacuum energy. Interesting proposals for all-optical dynamical Casimir effect came out in the context of three-level emitters [39] and intersubband excitations [26,40,41] controlled by strong resonant laser pulses. In the latter situation, the electron-hole polarization arising from transitions between the first and the second subbands of the quantum well (QW) conduction band is aligned along the z direction (perpendicular to the QW plane), and ultrastrongly coupled to a TM-polarized cavity mode [26,41]. A femtosecond control pulse suddenly promotes electrons from the valence band to the first subband of the QW conduction band, turning on the ultrastrong light-matter coupling. Although this proposal brings promising ideas for measuring the Casimir radiation induced by nonadiabatic switching of the ultrastrong light-matter interaction, several drawbacks exist. In addition to the experimental challenges stemming from the very short lifetimes of both electronic and photonic excitations, the presence of the Fermi sea in the conduction band with the possibility of creating low-energy excitations is likely to yield the Casimir photons absorption quickly after they are emitted. Aside from considering the possibility of using a multiple quantum well (MQW) structure sandwiched by 3D PBG material in order to increase the lifetime of photonic excitations, the other challenge when dealing with intersubband excitations is that the electric field in the z direction is strongly screened by the PBG material in the vicinity of the QWs, and provides much smaller coupling than in traditional microcavities. This prevents from achieving ultrastrong light-matter coupling in this case.

Recently, the cyclotron resonance in GaAs/AlGaAs QWs has been shown to yield very large coupling ratios $\Omega/\omega \sim 0.6$–0.9 at far-infrared frequencies $\omega = 500$ GHz–1 THz [42–45]. When a static magnetic field is applied perpendicularly to the 2D electron gas, the cyclotron resonance involving quantum states in adjacent, highly degenerate Landau levels (LLs) is coupled to the in-plane electric field of a cavity mode, and the system can be driven into the ultrastrong coupling regime [46]. Due to the harmonic oscillator spectrum, the dipole moment associated with a given LL n scales as $\sqrt{n}$. On the other hand, the Pauli exclusion principle implies that only electrons close to the Fermi level participate to the light-matter coupling and, hence, the VRF scales as $\sqrt{\nu}$, where ν denotes the LLs filling factor [46]. Similarly to microcavities used in the context of intersubband polaritons, the photon decay time does not exceed a few picoseconds in the metamaterial-based resonators used in those experiments [42–45], bringing up the idea of using 3D THz PBG materials with strong in-plane electric fields instead.

Considering the situation where ν is an integer number, i.e., quantum states in LLs with $n < \nu$ are completely filled and all the other ones with $n \geqslant \nu$ are empty, the electron-hole excitation spectrum is gapped and exhibits discrete horizontal lines with energies $p\hbar\omega_c$ ($p \in \mathbb{N}$), where ω_c denotes the cyclotron transition frequency corresponding to the separation between adjacent LLs. In addition to the possibility of achieving ultrastrong light-matter coupling in a 3D THz PBG, this system is thus an ideal candidate to observe the dynamical Casimir effect since there is no possible low-energy excitations that could lead to the absorption of Casimir photons. The crucial issue is now to find an efficient way of modulating the light-matter coupling parameters on short time scales. An interesting possibility is provided by recent advances in the generation of highly intense electromagnetic transients at THz frequencies, obtained by difference frequency generation with optical parametric amplifiers [47]. These pulses carry gigantic peak electric fields up to 108 MV cm^{-1} for short durations $\sim$250 fs, that can be used for control over charge and spin degrees of freedom in molecules and solids [48].

In this paper, we study the possibility of far-infrared ultrastrong coupling when a multiple GaAs/AlGaAs QW structure is sandwiched between 3D PBG material. In this situation, some 2D guided modes lying in the complete PBG are efficiently coupled to the cyclotron transition of the two-dimensional electron gas, when a static magnetic field is applied perpendicularly to the QW plane. We explore a new regime in which the photon damping is very low due to the 3D PBG, and the nonradiative damping of excitons is typically much larger due to the scattering with sample impurities and interface roughness in MQW structures. Nevertheless, the VRF is still larger thanks to the high filling factors $\nu \sim 10$ we consider here, allowing ultrastrong light-matter coupling. If an intense and few-cycle electromagnetic transient with a carrier frequency $\omega_p/(2\pi)$ is applied to the structure, the cyclotron transition frequency (proportional to the magnetic field) is modulated, cyclically tuned on and off resonance with a given photon guided mode, at the frequency $\omega_p/(2\pi)$. This provides an *in situ* modulation of the light-matter coupling, which in turn modifies the vacuum energy within the PBG-MQW structure. When the modulation frequency $\omega_p/(2\pi)$ is much larger than the bare excitations frequency (nonadiabatic modulation), Casimir photons are emitted out of the structure.

This paper is organized as follows. In Sec. II, we describe the physical system under consideration. In Sec. III, we derive the different contributions to the Hamiltonian and characterize the resulting polariton eigenmodes. The ultrafast time modulation of the magnetic field and the Casimir radiation spectrum are discussed in Sec. IV. In the Appendixes, we provide the detailed calculations of the light-matter Hamiltonian, polariton eigenstates, and Casimir photons spectrum. The employed numerical methods are discussed in the last Appendix.

II. PHYSICAL SYSTEM

A. MQW structure under magnetic field

We consider a MQW heterostructure based on GaAs material [25]. It consists of $n_{qw} = 70$ repetitions of 6.5-nm-wide

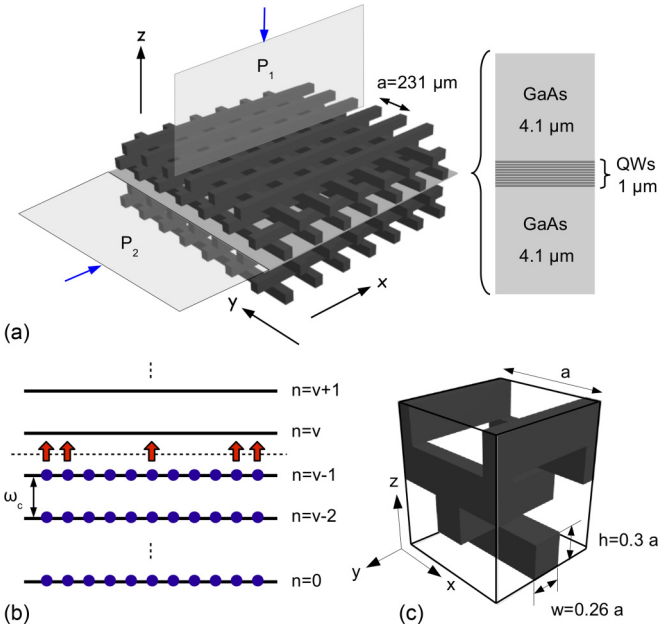

FIG. 1. (a) PBG-MQW structure consisting of a defect layer of thickness h_d (light gray) sandwiched by woodpile PBG material (dark gray). a is the lattice constant of the woodpile PBG material. The MQW structure (active region) of thickness 1 μm is sandwiched between two identical layers of GaAs of thickness 4.1 μm to comprise the total thickness of $h_d = 0.04a = 9.2$ μm (the lattice constant $a = 231$ μm is determined by imposing the resonance condition in Sec. II B 2). The two planes P_1 and P_2 represent the two cuts along which the spatial distribution of the y component of the electric field for the photon mode l_1 is represented in Fig. 4. (b) Sketch of LLs in the integer filling factor regime. The spacing $\hbar\omega_c$ between two adjacent, highly degenerate LLs is called the cyclotron gap. The last fully occupied LL is labeled by $n = \nu - 1$, and all higher-lying ones are completely empty at low temperature $k_BT \ll \hbar\omega_c$. The Fermi energy is defined as the energy level which has a probability $\frac{1}{2}$ of being occupied, and is represented as a dashed horizontal line lying in the middle of the cyclotron gap. (c) Unit cell of woodpile material, with size a in the x and y directions, and $1.2a$ in the z direction. The germanium logs have a thickness $h = 0.3a$, the first two (starting from the bottom) have a width $w = 0.26a$, and the two upper ones of width $w/2$ acquire the width w by repeating the unit cell in the two in-plane directions.

doped GaAs QWs, separated by 8-nm-wide $Al_{0.35}Ga_{0.65}As$ barriers. Each well contains a two-dimensional electron gas of density $\rho = 1.5 \times 10^{12}$ cm^{-2}, and the AlGaAs barriers are assumed large enough to neglect the overlap of the wave functions in adjacent QWs. The QW thickness is chosen such that only the first subband states are occupied for the given electron density ρ. This active region of thickness 1 μm is sandwiched between two identical bulk GaAs layers of thickness $\sim$4.1 μm in order to optimize the optical properties of the structure, as explained in the following. The slab is in turn sandwiched by germanium woodpile PBG material with lattice constant a. A static magnetic field $\mathbf{B} = B\mathbf{e}_z$ is applied along the z direction [Fig. 1(a)].

Cyclotron resonance involves transitions between the discrete LLs that arise from subjecting a two-dimensional electron gas to a perpendicular static magnetic field [49]. These LLs are separated from each other by the cyclotron frequency $\omega_c = eB/m^*$, where the influence of the host lattice potential is taken into account by replacing the bare electron mass m with the effective mass of the conduction band in the GaAs QWs: $m^* \approx 0.067$ m. Since the center of the cyclotron orbit, the so-called guiding center, can be located anywhere in the plane without energy cost, LLs are also highly degenerate. The magnetic length, associated with the cyclotron radius of the fundamental Landau level, is defined as $l_c = \sqrt{\hbar/(eB)}$, while the degeneracy of each LL is $N_\phi = S/(2\pi l_c^2)$, where $S = L^2$ is the surface of the 2D electron gas. Each LL is labeled by a positive integer n ($n = 0,1,2,\ldots$), as shown in Fig. 1(b). In the Landau's gauge, the static vector potential is given by $\mathbf{A} = Bx\mathbf{e}_y$, and the quantum number associated with the guiding center's degeneracy corresponds to the electron wave vector $k = 2\pi p/L$ ($p = 1,2,\ldots,N_\phi$) in the y direction. We consider the electron gas with integer filling factor ν, i.e., when the Fermi level lies between the last fully occupied LL $n = \nu - 1$ and the first empty one $n = \nu$, with $\nu = 2\pi l_c^2\rho$. For example, $\nu_0 = 50$ at $B_0 = 1.24$ T, which corresponds to a cyclotron transition of frequency $\omega_c^0/2\pi = 518$ GHz. For an electron gas with integer filling factor, the Pauli exclusion principle implies that only electrons from the last fully occupied LL $n = \nu - 1$ can undergo optical transitions at ω_c toward the first unoccupied one $n = \nu$ at low temperature $k_BT \ll \hbar\omega_c$ [Fig. 1(b)]. For sake of clarity, we perform the calculation in the zero-temperature limit for noninteracting electrons. Accordingly, we reduce the Hilbert space to the two active LLs $n = \nu - 1, \nu$. Since the absorption or emission of a photon is spin conserving, the cyclotron polarization coupled to photons involves only electrons and holes with the same spin. Consequently, the Zeeman splitting of LLs is reduced to a global energy shift and we can omit the spin degree of freedom.

An appropriate choice of the lattice constant $a = 231$ μm allows us to place the cyclotron transition of frequency $\omega_c^0/2\pi$ in resonance with a desired photonic mode. The electromagnetic field of this mode varies very slowly over the thickness of the active region (1 μm). The latter is then described as a single 2D electron gas with an effective density $n_{qw}\rho$. At this point, it is important to mention that we neglect the Hofstadter's spectrum [50] due to the periodic potential generated by the nearby 3D PBG material. Indeed, the coherence length of electrons in LLs does not exceed a few microns even at low temperature, and is then much smaller than the woodpile lattice constant a. The noninteracting ground state of electrons in LLs is written as

$$|F\rangle = \prod_{n=0}^{\nu-1}\prod_{p=1}^{N_\phi} c_{n,k}^\dagger\,|0\rangle\,, \tag{1}$$

where the operator $c_{n,k}$ ($c_{n,k}^\dagger$) annihilates (creates) a fermion in the LL n and guiding center k, and $|0\rangle$ corresponds to the vacuum state (absence of electrons). The fermion fields are expanded in terms of the one-electron wave functions as

$$\Psi(\mathbf{r}) = \sum_{n,k} \frac{e^{-iky}}{\sqrt{L}}\chi_{n,k}(x)\xi(z)c_{n,k}. \tag{2}$$

The confined motion along the z direction is described by the function $\xi(z)$, which stands for the first subband of the QW conduction band. The function $\chi_{n,k}(x)$ is given by

$$\chi_{n,k}(x) = \frac{1}{\sqrt{2^n n! l_c \sqrt{\pi}}} e^{-\frac{(x-kl_c^2)^2}{2l_c^2}} H_n\left(\frac{x-kl_c^2}{l_c}\right), \quad (3)$$

where H_n denotes the Hermite polynomial of order n. In this gauge, the electron wave functions are those of the one-dimensional (1D) harmonic oscillator shifted by the guiding center position kl_c^2. The second quantized Hamiltonian which represents the electron kinetic energy in presence of the static magnetic field is

$$H_0 = \sum_{n,k} \hbar\omega_c \left(n + \frac{1}{2}\right) c_{n,k}^\dagger c_{n,k}, \quad (4)$$

where we have dropped the constant energy of the QW conduction band.

B. Woodpile PBG material

The 3D woodpile structure made out of Group IV semiconductors has been successfully realized from centimeter [51,52] to submicron scales [53–56], using various techniques such as repetitive deposition/dry etching, microlithography/wet etching, dicing saw machining, or rapid prototyping based on polymer jetting [22]. It is formed by a stack of dielectric rectangular logs with alternating orthogonal orientations. In particular, the optimized four-layer structure with logs made out of germanium exhibits a complete band gap ~26% between the second and the third photonic bands. We assume that the relative dielectric permittivity of germanium is frequency independent in the range of interest and equal to $\epsilon = 16$. On the other hand, absorption losses in this material are small since the sample size is typically much smaller than the characteristic absorption length given by the inverse of the power attenuation coefficients in bulk germanium and gallium arsenide [respectively, $\alpha_{\mathrm{Ge}} \sim 1.5\ \mathrm{cm}^{-1}$ and $\alpha_{\mathrm{GaAs}} \sim 0.5\ \mathrm{cm}^{-1}$ at $\omega/(2\pi) = 500$ GHz [57]]. The optimized woodpile is characterized by the logs width $w = 0.26a$ and thickness $h = 0.3a$, where the lattice constant a corresponds to the center-to-center distance between two adjacent rods in a given layer [Fig. 1(c)]. The periodicity in the stacking direction z is $1.2a$. After an integer number of woodpile unit cells has been created, a defect layer of thickness $h_d = 0.04a$ is deposited. This defect layer consists of the active region previously described, sandwiched between two identical layers of GaAs to comprise the total thickness of $h_d = 0.04a$. The average dielectric constant of the defect layer $\epsilon_d = 13$ (mainly GaAs) is used to determine the electromagnetic properties of the structure. Finally, the deposition process of germanium woodpile logs is repeated on the top of the defect layer [Fig. 1(a)].

1. Infinite structure

Let us first consider that the sample previously described contains an infinite number of woodpile periods along the x and y directions. The defect layer is also considered as infinite in the xy plane. The whole structure preserves the discrete translational symmetry in the plane, but does not in the stacking direction z. This leads to the appearance of exponentially localized modes, confined near the defect layer in the z direction and propagating along the plane. These 2D guided modes, with a mixed TE and TM character, are characterized by an in-plane photon wave vector $\mathbf{q}$ in the first Brillouin zone, and a photonic band index m. Nevertheless, these modes are predominantly TE or TM, depending on the wave vector in the first Brillouin zone. The discrete translational symmetry in the plane imposes a set of reciprocal lattice vectors $\mathbf{G}$. Since the z component of the photon wave vector q_z is not a good quantum number, we consider the projection of the first Brillouin in the $q_z = 0$ plane. According to Bloch's theorem, the electric field Bloch functions consist of periodic functions $\mathbf{u}_{\mathbf{q},m}(\mathbf{r})$ modulated by plane-wave envelopes [12].

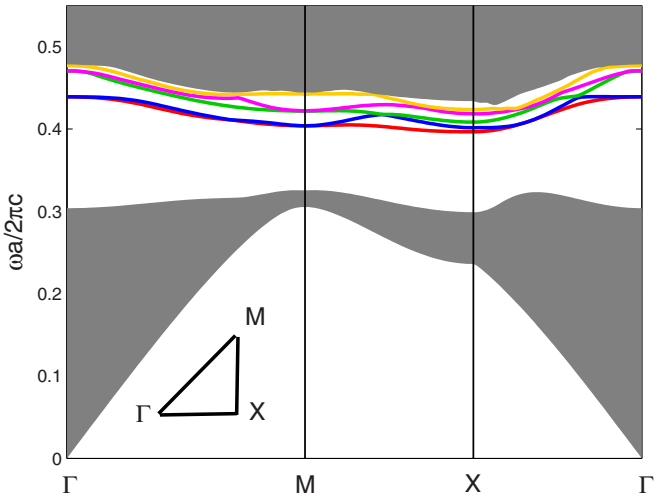

FIG. 2. The photonic band structure in the first Brillouin zone consists of the gray shaded region where extended electromagnetic modes can propagate in the bulk photonic crystal (woodpile structure), as well as five colored solid curves which correspond to the 2D guided modes propagating in the plane and localized in the vicinity of the defect slab. These modes are mainly polarized in the plane.

We have used a plane-wave expansion method (MPB software) to calculate the band structure and the electric field patterns corresponding to the different 2D guided modes present in the PBG. The supercell used in our simulation has a resolution of 64 points per lattice constant a, and includes 8 periods (32 logs) of woodpile in the stacking direction, 4 below the defect slab and 4 above it. Periodic boundary conditions are assumed in the xy plane. The corresponding band structure is represented on Fig. 2, in the first Brillouin zone. The shaded region contains the continuum of extended bands which can propagate in the 3D bulk woodpile. The white central region corresponds to the complete PBG, extending over the dimensionless frequency range $\frac{\Delta a}{2\pi c} = \frac{(\omega_> - \omega_<)a}{2\pi c} \sim 0.45$–$0.31$ ($\omega_>$ and $\omega_<$ denote, respectively, the upper and the lower band edge frequencies), and centered at $\frac{\omega_0 a}{2\pi c} = \frac{(\omega_> + \omega_<)a}{4\pi c} \sim 0.38$.

The solid colored curves represent the guided modes in which the periodic function $\mathbf{u}_{\mathbf{q},m}(\mathbf{r})$ ($\propto$ to the electric field) is mainly polarized in the xy plane. These modes are efficiently coupled to the cyclotron polarization. On the other hand, a few photonic bands mainly polarized in the stacking direction z actually lie in the narrow region between the fourth (purple)

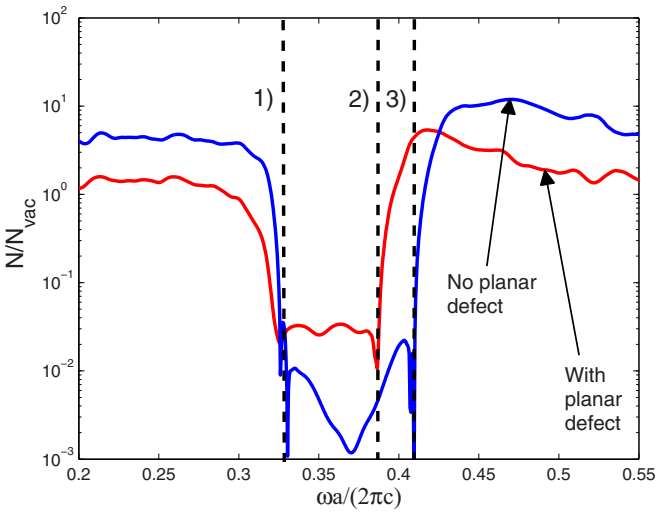

FIG. 3. Blue curve: local density of states $N(\mathbf{r}_0,\omega)$ of the PBG woodpile structure consisting of eight periods in the z direction and nine periods in the x and y directions (without defect layer), as a function of the normalized frequency. Red curve: local density of states $N(\mathbf{r}_0,\omega)$ of the PBG-MQW structure consisting of a defect layer of thickness $h_d = 0.04a$ sandwiched between four periods of woodpile material below and four periods above in the z direction. As for the blue curve, the structure consists nine woodpile unit cells in the x and y directions. The LDOS is normalized by the one in vacuum $N_{\rm vac}(\mathbf{r}_0,\omega)$, and the point r_0 is chosen in the middle of the structure along the z and x directions ($x_0 = z_0 = 0$), and at $y_0 = 0.14a$ in the y direction (Fig. 5). The vertical dashed lines indicate the lower and upper edges of the PBG.

band and the upper band edge. Since the coupling of these modes to the cyclotron transition is negligible at both Γ, X, and M points, they are not depicted.

2. Finite structure

We now consider the structure depicted in the beginning of Sec. II B, with a finite but large enough number of woodpile periods in both the stacking direction z and the xy plane. If $V = SL_z$ denotes the volume of the entire photonic crystal, we consider $S = (\gamma_S a)^2$ and $L_z = 4h\gamma_z + h_d$, with $\gamma_S = 9$ and $\gamma_z = 8$ in the following calculations. In this situation, the discrete translation invariance is broken in all directions and the photon spectrum consists of discrete modes. These modes are characterized by an index l such that the vector potential can be expanded in terms of the creation and annihilation photon operators $a_l^\dagger$ and a_l as

$$\mathbf{A}_{em}(\mathbf{r}) = \sum_l \sqrt{\frac{\hbar}{2\epsilon_0\omega_l}}(a_l\mathbf{u}_l(\mathbf{r}) + a_l^\dagger\mathbf{u}_l^*(\mathbf{r})), \tag{5}$$

where ω_l corresponds to the frequency of the mode l, ϵ_0 is the vacuum permittivity, and the electric field mode functions $\mathbf{u}_l$, solutions of the Maxwell equations, are normalized over the volume V of the entire photonic crystal as [58]

$$\int_V d\mathbf{r}\,\epsilon(\mathbf{r})\,\mathbf{u}_l^*(\mathbf{r})\cdot\mathbf{u}_{l'}(\mathbf{r}) = \delta_{l,l'}. \tag{6}$$

$\epsilon(\mathbf{r})$ represents the position-dependent relative dielectric constant. An interesting quantity to look at is the projected local photonic density of states $N(\mathbf{r}_0,\omega)$, proportional to the power spectrum of a radiating dipole at a given point $\mathbf{r}_0$:

$$N(\mathbf{r}_0,\omega) = \sum_l \delta(\omega-\omega_l)\epsilon(\mathbf{r}_0)|\mathbf{u}_l(\mathbf{r}_0)|^2, \tag{7}$$

where $\mathbf{u}_l$ denotes the electric field profile in the direction of the radiating dipole. In Fig. 3, we have represented the local density of states (LDOS) obtained by a finite-difference time-domain (FDTD) calculation (see Appendix D), normalized by the photonic density of states in vacuum

$$N_{\rm vac}(\mathbf{r}_0,\omega) = \frac{\omega^2}{6\pi^2c^3}, \tag{8}$$

projected in an arbitrary direction. c represents the speed of light in vacuum. We consider a point dipole source with a broad spectrum aligned in the direction $\mathbf{e}_x + \mathbf{e}_y$, and placed at point $\mathbf{r}_0$ defined in Fig. 5.

The blue curve corresponds to the LDOS for the structure just described, but without the defect layer (perfect woodpile structure). As expected, in the frequency range delimited by the black dashed lines 1 and 3, the LDOS is very small, indicating the presence of the complete photonic band gap. The finite size of the structure along the three spatial directions implies that the LDOS is not strictly zero in the PBG, even if it becomes exponentially small for a large enough number of woodpile periods. The red curve represents the LDOS for the structure containing the defect layer of thickness $h_d = 0.04a$ sandwiched between between four periods of woodpile material below and four periods above in the z direction. In the region delimited by the black dashed lines 2 and 3, the presence of the defect layer leads to a LDOS enhancement in the PBG, close to the upper band edge, which is due to the presence of the guided modes.

A FDTD calculation detailed in Appendix D allows us to determine the mode functions $\mathbf{u}_l(\mathbf{r})$ with frequency ω_l. We find that four of them with normalized frequencies $2\pi c0.39/a$, $2\pi c0.4/a$, $2\pi c0.42/a$, and $2\pi c0.43/a$ exhibit particularly strong in-plane electric fields and are thus efficiently coupled to the cyclotron polarization [the z components $u_l^z(\mathbf{r})$ are negligible]. These modes are labeled by the indices l_1,l_2,l_3,l_4, and we will neglect all the other dark modes in the vector potential modal expansion (5). The spatial distribution of the y component of the electric field corresponding to the mode l_1 is represented in Fig. 4. The electromagnetic energy of the four dominant guided modes in the finite-size structure can be written as

$$H_{pc} = \sum_{l=l_1}^{l_4}\hbar\omega_l\left(a_l^\dagger a_l + \frac{1}{2}\right). \tag{9}$$

If the cyclotron transition at $B_0 = 1.24$ T is resonant with l_1, the relation $2\pi c\,0.39/a = \omega_c$ requires that $a = 231$ μm for $\omega_c^0/(2\pi) = 518$ GHz, as mentioned in Sec. II A. The total thickness of the defect layer is $h_d = 0.04a = 9.2$ μm, with the active region (of thickness 1 μm) sandwiched between two 4.1-μm-thick GaAs layers.

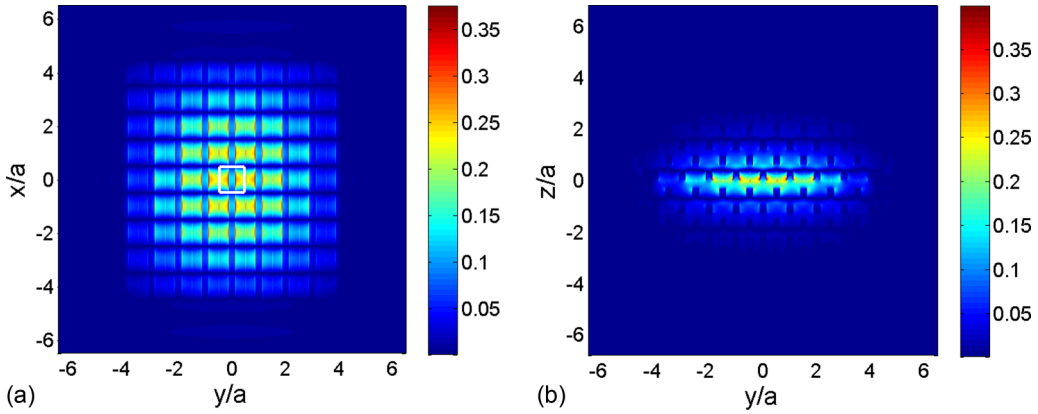

FIG. 4. Spatial distribution $u^y_{l_1}(\mathbf{r})$ of the y component of the electric field for the photon mode l_1. It is represented as a function of the x and y coordinates at $z = 0$ in (a) [plane P_2 in Fig. 1(c)], and as a function of y and z at $x = 0$ in (b) [plane P_1 in Fig. 1(c)]. The white square in the middle of (a) represents the central unit cell (see Fig. 5).

III. PBG POLARITONS

Our method of generating Casimir photons is by modulating the cyclotron gap ω_c using an intense electromagnetic transient that impinges the MQW structure at point $\mathbf{r}_0$ where the guided modes magnitude reaches its maximum. In order to achieve the strong magnetic fields required for this operation, the beam has to be focused on a small surface of the defect layer (pulse cross section in Fig. 5) considered as a disk of surface $s = \pi(d_p/2)^2$ and centered at point $\mathbf{r}_0$, with $d_p \sim 10\ \mu$m much larger than the cyclotron length $l_c \sim 20$ nm at $B_0 = 1.24$ T, but also much smaller that the lattice constant $a \sim 230\ \mu$m. In the following, we will consider that only electrons in the surface s are optically active in the sense that the cyclotron gap can be controlled within this surface. The electromagnetic pulse is considered as a plane wave with its electric field polarized along the y direction and its magnetic field contained in the xz plane (Fig. 5).

A. Light-matter Hamiltonian

We begin with a static magnetic field B applied to the finite structure described above. In presence of the static vector potential $\mathbf{A} = Bx\mathbf{e}_y$ as well as the electromagnetic one $\mathbf{A}_{em}$, the microscopic light-matter coupling Hamiltonian is obtained by replacing the linear momentum $\boldsymbol{p}$ by the quantity $\boldsymbol{\pi} + e\mathbf{A}_{em}(\mathbf{r})$ in the expression of the bare kinetic energy. $\boldsymbol{\pi} = \mathbf{p} + e\mathbf{A}$ corresponds to the conjugate momentum that diagonalizes the kinetic energy in the presence of a static vector potential $\mathbf{A}$. Calling V_{conf} the QW confinement potential, we obtain

$$\mathcal{H} = \frac{1}{2m^*}(\boldsymbol{\pi} + e\mathbf{A}_{em})^2 + V_{\text{conf}}(z). \tag{10}$$

This Hamiltonian can be separated into three parts. The first one $\frac{\boldsymbol{\pi}^2}{2m^*} + V_{\text{conf}}(z)$ corresponds to the LLs Hamiltonian (4) for bare electrons in the QW conduction band. The second part involves the linear coupling between the momentum $\boldsymbol{\pi}$ and the electromagnetic vector potential $\mathbf{A}_{em}$. Using the fermion fields in Eq. (2), the second quantized Hamiltonian which corresponds to the linear coupling is written as

$$H_I = \frac{e}{m^*}\int_{\delta\mathbf{r}_0} d\mathbf{r}\, \Psi^\dagger(\mathbf{r})\mathbf{A}_{em}\cdot\boldsymbol{\pi}\Psi(\mathbf{r}). \tag{11}$$

The volume $\delta\mathbf{r}_0$ consists of the disk of surface s centered at point $\mathbf{r}_0$ in the xy plane and of the QW region along the z direction. After some calculations that are detailed in Appendix A, this Hamiltonian can be put on the form

$$H_I = \sum_l \hbar\Omega_l(b + b^\dagger)(a_l + a_l^\dagger), \tag{12}$$

where the coupling constant associated with the photon mode l is derived as

$$\Omega_l = \sqrt{\frac{e^2 n_{qw}\rho\,\omega_c}{4\epsilon_0 m^*\omega_l a}} \times \widetilde{u}_l(\mathbf{r}_0). \tag{13}$$

The cyclotron polarization is coupled to the in-plane modes

$$\widetilde{u}_l(\mathbf{r}_0) = iu^x_l(\mathbf{r}_0) + u^y_l(\mathbf{r}_0), \tag{14}$$

where u^j_l $(j = x,y)$ denotes the j component of the mode function $\mathbf{u}_l$. Note that the FDTD calculation shows that the x component $u^x_l(\mathbf{r}_0)$ at point $\mathbf{r}_0$ is negligible for all l, and thus $\widetilde{u}_l(\mathbf{r}_0) \approx u^y_l(\mathbf{r}_0)$. The coupling Hamiltonian (12) involves the

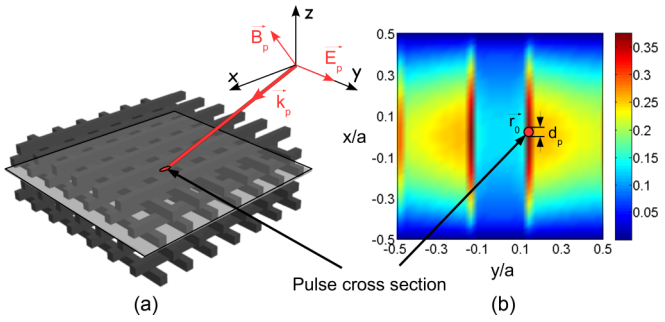

FIG. 5. (a) An intense electromagnetic pulse impinges the MQW structure at point $r_0 \equiv (0,0.14,0)a$. The pulse electric field $\mathbf{E}_p$ is polarized along the y direction, and the magnetic field $\mathbf{B}_p$ is polarized in the xz plane. (b) Spatial profile $u^y_{l_1}(\mathbf{r})$ of the y component of the electric field for the photon mode l_1 represented in the xy plane at $z = 0$, in the central unit cell corresponding to the white square in Fig. 4. The pulse cross section is considered as a red disk of diameter d_p.

so-called magnetoexciton (MX) operator

$$b^\dagger = \frac{1}{\sqrt{N_\phi}} \sum_k c^\dagger_{\nu,k} c_{\nu-1,k}, \tag{15}$$

and its Hermitian conjugate b. These operators, respectively, create and annihilate a collective excitation, superposition of electron-hole pairs between the last fully occupied LL and the first empty one. They obey bosonic commutation relations $\langle F|[b,b^\dagger]|F\rangle = 1$ in the subspace spanned by the noninteracting ground state $|F\rangle$. Moreover, restricting the Hilbert space to quantum states which contain at most one MX (dilute regime), we can consider the corresponding operators as bosonic [59]. The contributions proportional to $b^\dagger a_l$ and $b a_l^\dagger$ are denoted as "rotating wave" contributions, while $b^\dagger a_l^\dagger$ and $b a_l$ are denoted as "counter-rotating" contributions. The latter are neglected in the strong coupling regime (rotating wave approximation). Using the results of the FDTD calculation for ω_l and $\widetilde{u}_l(\mathbf{r}_0)$ (Sec. II B 2 and Appendix D), the vacuum Rabi frequencies in Eq. (13) are evaluated as $\Omega_{l_1}/\omega_c^0 \approx \Omega_{l_2}/\omega_c^0 = 0.82$, $\Omega_{l_3}/\omega_c^0 = 0.88$, and $\Omega_{l_4}/\omega_c^0 = 0.54$. These large coupling ratios show that the ultrastrong coupling regime is achieved.

B. Magnetoexcitons

In the previous section, we have seen that the light-matter coupling Hamiltonian can be expressed in terms of the MX operators $b^\dagger$ (b), bosonic in the low excitation density regime. Unlike interband excitons, they do not form hydrogenic bound states because LLs in the first subband are characterized by the same band effective mass m^*. In presence of Coulomb interactions, the long-wavelength ($\gg l_c$) excitation spectrum is dominated by a coherent plasmon mode with frequency ω_c, and often referred to as depolarization shift [60]. The absence of Coulomb corrections for long-wavelength excitations can be seen as a consequence of the Kohn's theorem [61], which asserts that the cyclotron resonance of a translationally invariant 2D electron gas in a uniform static magnetic field occurs at $\omega = \omega_c$ when probed by a long-wavelength radiation, regardless of Coulomb electron-electron interactions. For a slowly varying electric field with wavelength $\sim a \gg l_c$, the plasmon mode corresponds to a quasihomogeneous polarization of the electron gas, free from Coulomb scattering. This plasmon is ultrastrongly coupled to the in-plane electric field confined in the 3D PBG material. The effective Hamiltonian which describes the kinetic energy in terms of MXs can thus be written as

$$H_{ex} = \hbar\omega_c b^\dagger b. \tag{16}$$

In real samples at low temperature, elastic scattering due to QW interface roughness and dopant impurities dominates the linewidth of MXs [62], depending strongly on physical parameters such as electron areal density, filling factor, magnetic field, and electron mobility at $B = 0$. In this paper, we consider an active region containing 70 narrow and highly doped QWs, which places us in a regime where MXs typically have a short lifetime $\lesssim 1$ ps [62]. However, we will see that some of the polaritons resulting from the ultrastrong light-matter coupling have a very small MX weight. Their lifetimes are thus dominated by the photon mode ones, which are much longer ($\sim$1 ns) due to the 3D PBG.

C. $\mathbf{A}^2_{em}$ contribution

The last contribution of the microscopic Hamiltonian (10) is proportional to the square electromagnetic vector potential $\mathbf{A}^2_{em}$. In second quantization, the corresponding Hamiltonian can be written as

$$\mathcal{H}_{II} = \frac{e^2}{2m^*} \int_{\delta\mathbf{r}_0} d\mathbf{r}\, \Psi^\dagger(\mathbf{r}) \mathbf{A}^2_{em}(\mathbf{r}) \Psi(\mathbf{r}). \tag{17}$$

We insert Eqs. (2) and (5) into (17), and after a calculation detailed in Appendix A, we obtain

$$H_{II} = \sum_{l,l'} \hbar D_{l,l'} (a_l + a_l^\dagger)(a_{l'} + a_{l'}^\dagger), \tag{18}$$

where the coupling amplitude reads as

$$D_{l,l'} = \frac{\Omega_l \Omega_{l'}}{\omega_c}. \tag{19}$$

This purely photonic contribution yields a mixing between the different photon modes, and does not depend on the applied magnetic B. It can be diagonalized together with the electromagnetic energy (9), and gives a blue-shift of the guided mode energy which depends only on the effective electron density $n_{qw}\rho$. Unlike the strong coupling situation where the VRF is much smaller than the bare excitation frequencies, this term cannot be neglected in the ultrastrong coupling regime. Moreover, it prevents the system from Dicke-type instabilities thanks to the fact that the total Hamiltonian consisting of the contributions (9), (12), (16), and (18) is positive definite for all possible values of Ω_l. This is not the case in absence of the contribution (18), and the model exhibits a quantum critical point [63].

D. Polariton dispersion

We can now proceed with the numerical diagonalization of the polariton Hamiltonian

$$\begin{aligned} H_{\rm pol} = &\sum_l \hbar\omega_l \left(a_l^\dagger a_l + \frac{1}{2}\right) + \hbar\omega_c b^\dagger b \\ &+ \sum_l \hbar\Omega_l (b + b^\dagger)(a_l + a_l^\dagger) \\ &+ \sum_{l,l'} \hbar D_{l,l'} (a_l + a_l^\dagger)(a_{l'} + a_{l'}^\dagger), \end{aligned} \tag{20}$$

which consists of the bare modes energy (9), the linear part of the coupling (12), the MX energy (16), and the $\mathbf{A}^2_{em}$ term (18). We introduce the so-called polariton annihilation operators [64]

$$p_\lambda = \sum_l W_{l,\lambda} a_l + Y_{l,\lambda} a_l^\dagger + X_\lambda b + Z_\lambda b^\dagger \tag{21}$$

and the creation operator $p_\lambda^\dagger$. These operators involve mixed combinations of MXs and photonic excitations. In particular, X_λ and $W_{l,\lambda}$ are associated with the rotating wave contributions in Eq. (12) and correspond, respectively, to the MX and photon

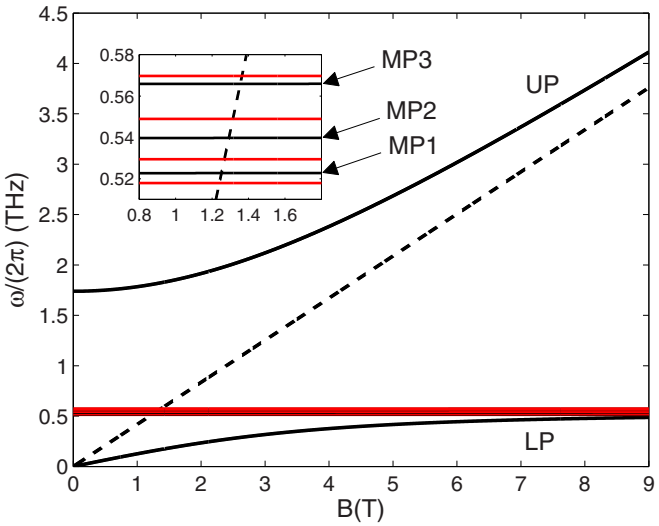

FIG. 6. Polariton frequencies $\omega_\lambda/(2\pi)$ in THz (black solid curves) as a function of the applied magnetic field B (in Tesla) in the z direction. LP and UP stand, respectively, for lower and upper polaritons, and MP1, MP2, MP3 for the three middle polaritons. The horizontal red solid lines correspond to the photon guided mode frequencies $\omega_{l_j}/(2\pi)$, with $j = 1,2,3,4$, and the cyclotron transition frequency ω_c is represented as a black dashed line. Inset: same quantities represented in a narrow frequency range corresponding to the crossing region where the resonance occurs. The cyclotron transition is resonant with the photon mode l_1 at $B_0 = 1.24$ T.

weights of the polariton λ. On the other hand, Z_λ and $Y_{l,\lambda}$ are associated with the counter-rotating contributions (neglected in the rotating wave approximation) and are respectively related to the MXs and photonic populations contained in the light-matter ground state $|G\rangle$, defined as $p_\lambda |G\rangle = 0$ [24]. The normalization condition

$$\sum_l |W_{l,\lambda}|^2 + |X_\lambda|^2 - \sum_l |Y_{l,\lambda}|^2 - |Z_\lambda|^2 = 1 \qquad (22)$$

is imposed by the bosonic commutation relation $[p_\lambda, p_\lambda^\dagger] = 1$. The Hamiltonian can be written in a diagonal form

$$H_{\rm pol} = \sum_\lambda \hbar\omega_\lambda p_\lambda^\dagger p_\lambda + \sum_\lambda \frac{\hbar\omega_\lambda}{2}, \qquad (23)$$

and the coefficients entering Eq. (21) are given by the solutions of the eigenvalue equation $[p_\lambda, H_{\rm pol}] = \hbar\omega_\lambda p_\lambda$. As detailed in Appendix B, this eigenvalue problem can be put in a matrix form, which we propose to diagonalize numerically. In our calculation, we include the four guided modes with electric fields mainly polarized in the xy plane. In Fig. 6, we have represented the polariton frequencies $\omega_\lambda/(2\pi)$ ($\lambda = 1,2,\ldots,5$) as a function of the applied magnetic field B (black solid curves). The cyclotron transition of frequency $\omega_c^0/(2\pi) = 518$ GHz ($B_0 = 1.24$ T) is resonant with the photon mode l_1. In addition to the so-called lower and the upper polariton (LP and UP, respectively) which exhibit the usual polariton anticrossing, the three other polariton branches (middle polaritons MP1, MP2, MP3) are very weakly shifted from the photon guided modes of frequencies $\omega_l/(2\pi)$ (horizontal red solid lines) and very weakly varying with the magnetic field.

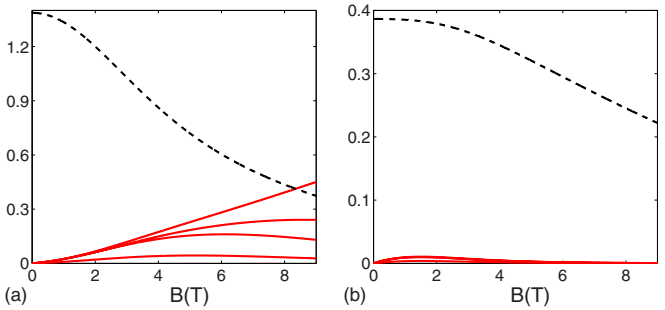

FIG. 7. Square modulus of the Bogoliubov transformation coefficients entering Eq. (21) for the LP as a function of the applied magnetic field. (a) Coefficients associated with the rotating wave contributions: $|X_{\rm LP}|^2$ for the MX weight (black dashed curve) and $|W_{l,{\rm LP}}|^2$ with $l = l_1,l_2,l_3,l_4$ for the photon weights (red solid curves). (b) Coefficients associated with the counter-rotating contributions: $|Z_{\rm LP}|^2$ for the MX (black dashed curve) and $|Y_{l,{\rm LP}}|^2$ with $l = l_1,l_2,l_3,l_4$ for the photon modes (red solid curves).

It is interesting to look at the transformation coefficients for the different polariton branches λ. In Figs. 7, 8, and 9, we have represented the square modulus of these coefficients as a function of the applied magnetic field B for $\lambda = {\rm LP}$, $\lambda = {\rm MP2}$, and $\lambda = {\rm UP}$, respectively. The (a) panels correspond to the coefficients associated with the rotating wave contributions: $|X_\lambda|^2$ for the MX weight (black dashed curve), and $|W_{l,\lambda}|^2$ ($l = l_1,l_2,l_3,l_4$) for the photon weights (red solid curves). The LP and the UP are hybrid quantum states partly MXs and photons. Moreover, at small magnetic field $B \sim 1$ T, the LP and the UP are, respectively, dominated by their exciton and photon weights, and the opposite situation at high magnetic field $B \gg 1$ T. Importantly, the middle polariton MP2 has a negligible MX weight regardless of the magnetic field [Fig. 8(a)]. The same property stands for MP1 and MP3. These branches are actually hybrid states mixing only the different photon modes l together. The (b) panels represent the coefficients associated with the counter-rotating contributions: $|Z_\lambda|^2$ for the MX (black dashed curve) and $|Y_{l,\lambda}|^2$ ($l = l_1,l_2,l_3,l_4$) for the photon guided modes (red solid curves). The populations of excitons and photon modes contained in the ground state $|G\rangle$ are equal to the square modulus of these coefficients (summed over the different polariton branches), i.e., $\langle G|\, b^\dagger b\, |G\rangle = \sum_\lambda |Z_\lambda|^2$ and $\langle G|\, a_l^\dagger a_l\, |G\rangle = \sum_\lambda |Y_{l,\lambda}|^2$. Both the LP and the UP exhibit rather large counter-rotating coefficients close to resonance,

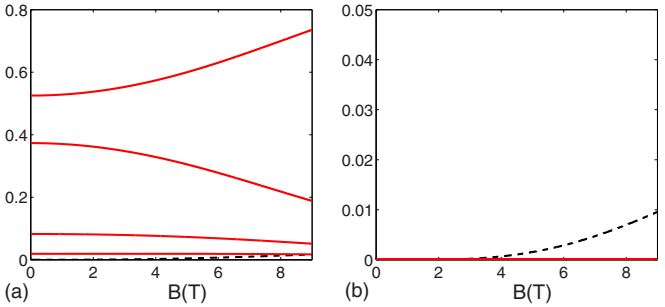

FIG. 8. Same quantities as in Fig. 7, for the middle polariton MP2. MP1 and MP3 exhibit similar coefficients.

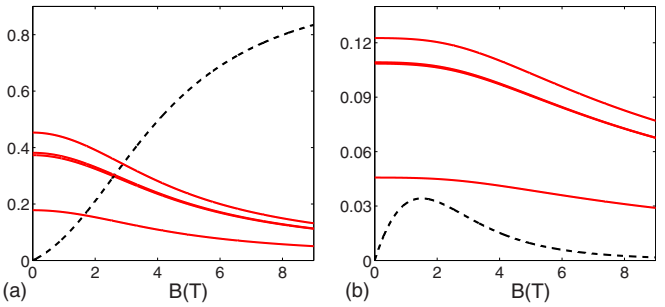

FIG. 9. Same quantities as in Figs. 7 and 8, for the upper polariton UP.

indicating squeezing effects characteristic of the ultrastrong coupling regime [24]. In particular, these contributions do not vanish at $B = 0$. This is due to the presence of the $\mathbf{A}_{em}^2$ term which amplitude $D_{l,l'}$ does not depend on the magnetic field, unlike the other contributions (12) and (16) which vanish at $B = 0$. Moreover, the counter-rotating coefficients for the MPs are very small, which means that these states are well described by hybrid states of the form $p_{\mathrm{MP2}} = \sum_l W_{l,\mathrm{MP2}}\, a_l$, and similar expressions for MP1 and MP3.

IV. DYNAMICAL CASIMIR EFFECT

The dynamical Casimir effect is a photon emission which occurs by changing the vacuum properties on a short time scale, typically much shorter than the period of the electromagnetic modes composing this vacuum. Let us assume that we are able to change the applied magnetic field B during a much smaller time scale than the period $2\pi/\omega_l$ of the photon guided modes coupled to the cyclotron transition. The polariton Hamiltonian is then given by Eq. (20), with the time-dependent parameters $\omega_c(t)$ and $\Omega_l(t)$. From Eq. (23), we can see that the energy of the ground state $E_G = \langle G|\, H_{\mathrm{pol}}\, |G\rangle$ depends on the applied magnetic field $B(t)$, which means that modulating the magnetic field allows us to change the vacuum energy, and the emission of Casimir photons is thus expected to occur. We point out that this is different from dynamical Stark effects, where the electronic energy levels are split due to the dipolar coupling with a time-varying electric field. In our proposal, we use a time-varying magnetic field to detune the cyclotron transition frequency, which in turn modifies the coupling to the photon guided modes. Since vacuum properties directly depend on this coupling, the former can thus be modulated on an ultrashort time scale resulting in the emission of Casimir photons. From Eq. (13), we see that $\Omega_l(B) \propto \sqrt{B}$. This means that the modification of the light-matter coupling when changing the magnetic field is dominated by the detuning of the cyclotron frequency $\omega_c(B) \propto B$ rather than by the change in the coupling constants $\Omega_l(B)$ themselves.

A. Ultrafast modulation

The strong magnetic fields required for this operation can be obtained by difference-frequency generation with optical parametric amplifiers [47]. This technology allows to generate intense few-cycle electromagnetic transients in the THz frequency range, with maximum peak electric fields of

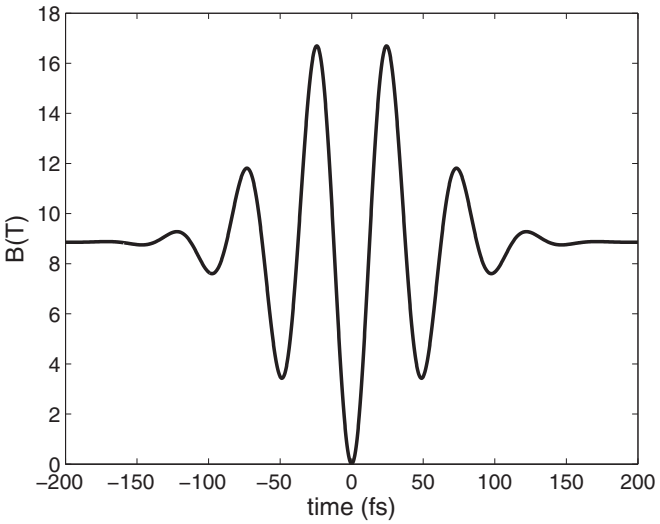

FIG. 10. Total magnetic field along the z direction $B(t) = B_i + B_p^z(t)$ where $B_p^z(t)$ is given by Eq. (24) as a function of time (in femtoseconds). Parameters are $\Delta t = 50$ fs and $\omega_p/(2\pi) = 20$ THz. Before the pulse is applied, we have $B(t = -\infty) \equiv B_i = 8.86$ T. At $t = 0$, the total magnetic field vanishes, i.e., $B(0) = 0$. The pulse duration is $\sim$250 fs, and after the latter is turned off, the total magnetic field comes back to its initial value $B(t = +\infty) \equiv B_i$.

108 MV cm^{-1} and magnetic fields $\sim$33 T. Let us consider the system initially subjected to a static magnetic field $B_i = 8.86$ T such that $\nu_i = 7$, at $t = -\infty$. The cyclotron transition frequency is $\omega_c^i/(2\pi) = 3.7$ THz. An intense electromagnetic pulse is then applied to the structure (Fig. 5). According to Ref. [47], the z component of the pulse magnetic field $B_p^z(t)$ consists of a Gaussian envelope of full width at half maximum $= 2\Delta t\sqrt{2\ln 2} \approx 118$ fs with $\Delta t = 50$ fs $\ll 2\pi/\omega_l \approx 1.9$ ps, modulated by a sinusoidal function oscillating at ω_p:

$$B_p^z(t) = -B_i \cos(\omega_p t) e^{-\frac{t^2}{2\Delta t^2}}. \tag{24}$$

The maximum peak amplitude $-B_i$ is chosen such that the total magnetic field (along the z direction) $B(t) = B_i + B_p^z(t)$ vanishes at $t = 0$ (Fig. 10). Using Eq. (24) and expanding the square root in Eq. (13), we can now write the time-dependent cyclotron transition frequency and the VRF as $\omega_c(t) = \omega_c^i + \Delta\omega_c(t)$ and $\Omega_l(t) = \Omega_l^i + \Delta\Omega_l(t)$, with

$$\begin{aligned}
\Delta\omega_c(t) &= \frac{e\Delta B}{m^*} \cos(\omega_p t) e^{-\frac{t^2}{2\Delta t^2}}, \\
\Delta\Omega_l(t) &= \Omega_l^i \sum_{p=1}^{+\infty} \frac{(-1)^p (2p)!}{(1-2p)(p!)^2 (4^p)} \left(\frac{\Delta B}{B_i} \cos(\omega_p t) e^{-\frac{t^2}{2\Delta t^2}} \right)^p,
\end{aligned} \tag{25}$$

and the VRF in the initial state

$$\Omega_l^i = \sqrt{\frac{e^2 n_{qw} \rho\, \omega_c^i}{4\epsilon_0 m^* \omega_l a}} \times \widetilde{u}_l(\mathbf{r}_0). \tag{26}$$

B. In-plane electric field

In addition to the magnetic field $B_p^z(t)$, the electromagnetic transient also carries a strong electric field in the y direction

$$E_p^y(t) = -E_i \cos(\omega_p t) e^{-\frac{t^2}{2\Delta t^2}}, \tag{27}$$

with $E_i = B_i c \approx 26.6\ \mathrm{MV\,cm^{-1}}$, and where the magnetic field $\mathbf{B}_p(t)$ is assumed to make an angle $\pi/4$ with the x and z axes. This electric field not only exceeds the electrical breakdown of the semiconductor material, but can also induce transitions between the LLs, preventing the stability of the ground state during the perturbation. Nevertheless, the pulse duration is extremely short, and if the overlap between its spectrum and the cyclotron resonance at ω_c^i is small enough, the probability for an electron belonging to the LL $n = \nu - 1$ to go in the next LL $n = \nu$ under the influence of the pulse electric field perturbation can be made much smaller than one. Given that $\Delta t \ll \frac{2\pi}{\omega_c^i}$, this probability can be calculated using time-dependent perturbation theory as

$$P_c = \left| \frac{e l_c^i \sqrt{\nu_i}}{i\hbar\sqrt{2}} \int dt\, e^{i\omega_c^i t} E_p^y(t) \right|^2 \approx \left(\frac{e l_c^i \sqrt{\pi \nu_i}\, \Delta t\, \Delta E}{\hbar} e^{-\omega_p \Delta t} \right)^2, \tag{28}$$

with $l_c^i = \sqrt{\hbar/(eB_i)}$ and $\nu_i = 2\pi (l_c^i)^2 \rho$. This function decreases very rapidly toward zero around $\omega_p/(2\pi) = 15$ THz. Consequently, if we choose the value of the pulse modulation frequency $\omega_p/(2\pi)$ so that it is larger than 15 THz, the effect of the pulse electric field perturbation can be safely neglected. We will consider $\omega_p/(2\pi) = 20$ THz in the following calculations.

C. Emitted photon spectrum

In this section, we calculate the photon spectrum emitted by dynamical Casimir effect in the framework of the quantum Langevin model including dissipation reservoirs [65,66]. This method treats differently the four in-plane-polarized guided modes strongly coupled to the cyclotron polarization on one hand, and all the other electromagnetic modes of the structure forming a quasicontinuum on the other hand. We assume that this continuum can be described by introducing four statistically independent photonic reservoirs weakly interacting with the four photon guided modes, and giving the latter finite lifetimes. In addition to the photon damping, MXs are scattered by lattice phonons, impurities, and interface roughness of the MQW structure. These nonradiative dissipative processes are taken into account in a similar fashion. Namely, we consider another bosonic reservoir weakly interacting with the MXs and giving them a finite lifetime. The total Hamiltonian in presence of dissipation is $H = H_{\mathrm{pol}} + H_{\mathrm{bath}}^{ph} + H_{\mathrm{bath}}^{ex}$, where

$$\begin{aligned} H_{\mathrm{bath}}^{ph} &= \sum_{\eta_l} \hbar\omega_{\eta_l} a_{\eta_l}^\dagger a_{\eta_l} + \sum_{\eta_l} \hbar\kappa_{\eta_l} a_l^\dagger a_{\eta_l} + \hbar\kappa_{\eta_l}^* a_l a_{\eta_l}^\dagger, \\ H_{\mathrm{bath}}^{ex} &= \sum_{\mu} \hbar\omega_\mu b_\mu^\dagger b_\mu - \sum_{\mu} \hbar\kappa_\mu b^\dagger b_\mu + \hbar\kappa_\mu^* b b_\mu^\dagger. \end{aligned} \tag{29}$$

ω_{η_l} and ω_μ are the frequencies of the reservoir excitations, while κ_{η_l} and κ_μ denote, respectively, the tunneling matrix elements for a photon mode l and for a MX to leak in the associated baths. The bath operators b_μ and a_{η_l} satisfy the bosonic commutation relations. As detailed in Appendix C, we solve the equations of motion in the Heisenberg picture for the photon and MX opetators a_l and b. Important physical quantities of the model are the Fourier transforms $\Gamma_{ex}(\omega)$ and $\Gamma_{ph}^l(\omega)$ of the memory kernels

$$\begin{aligned} \Gamma_{ex}(t) &= \Theta(t) \sum_{\mu} |\kappa_\mu|^2 e^{-i\omega_\mu t}, \\ \Gamma_{ph}^l(t) &= \Theta(t) \sum_{\eta_l} |\kappa_{\eta_l}|^2 e^{-i\omega_{\eta_l} t} \end{aligned} \tag{30}$$

for the MX and each photonic mode l, respectively. The real parts of the Fourier transforms are related to dissipation and correspond to the damping rates:

$$\begin{aligned} \mathrm{Re}\Gamma_{ex}(\omega) &= \sum_{\mu} \pi |\kappa_\mu|^2 \delta(\omega - \omega_\mu), \\ \mathrm{Re}\Gamma_{ph}^l(\omega) &= \sum_{\eta_l} \pi |\kappa_{\eta_l}|^2 \delta(\omega - \omega_{\eta_l}). \end{aligned} \tag{31}$$

The imaginary parts correspond to the Lamb shifts of the bare excitation energies ω_c and ω_l due to the coupling to the reservoirs, and are related to the damping rates by the Kramer-Kronig relations

$$\begin{aligned} \mathrm{Im}\Gamma_{ex}(\omega) &= -\frac{1}{\pi} \mathrm{p.v.} \int_{-\infty}^{+\infty} d\omega' \frac{\mathrm{Re}\Gamma_{ex}(\omega')}{\omega' - \omega}, \\ \mathrm{Im}\Gamma_{ph}^l(\omega) &= -\frac{1}{\pi} \mathrm{p.v.} \int_{-\infty}^{+\infty} d\omega' \frac{\mathrm{Re}\Gamma_{ph}^l(\omega')}{\omega' - \omega}, \end{aligned} \tag{32}$$

where p.v. denotes the Cauchy principal value. The usual and simplest way of including dissipation is the Markov approximation, that is considering frequency-independent damping rates. Back in the equations of motion, this leads to an exponential decay of the fields. In order to describe the loss of quantum coherence of MXs due to nonradiative processes, we consider a constant damping rate $\mathrm{Re}\Gamma_{ex}(\omega) \equiv \Theta(\omega)\Gamma_{ex}$ in the framework of the Markov approximation. The Heaviside function $\Theta(\omega)$ is introduced because the reservoir excitations have positive frequencies $\omega_\mu > 0$. Regarding the photon damping, the Markov approximation is relevant in the case of metallic cavities and semiconductor waveguides [65,66], where the photonic density of states is proportional to the one in vacuum [see Eq. (8)].

In our system, however, the presence of a complete PBG leads to a drastic, qualitative change of the LDOS (Sec. II B 2), and the Markov approximation breaks down [67]. Thus, we assume frequency-dependent damping rates for each photonic mode l, reproducing the LDOS variations calculated in the woodpile structure without planar defect (blue curve in Fig. 3). This mimics the electromagnetic environment experienced by the guided modes propagating in the defect layer. We define the PBG photon damping rates as

$$\mathrm{Re}\Gamma_{ph}^l(\omega) = \Theta(\omega) \left(\Gamma_{ph}[1 - \mathrm{R}(\omega - \omega_0)] + \frac{\mathrm{R}(\omega - \omega_0)}{\tau_l} \right), \tag{33}$$

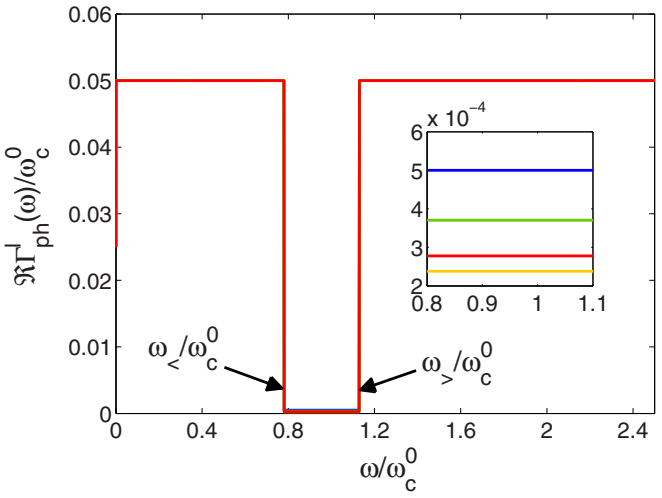

FIG. 11. Damping rates $\mathrm{Re}\Gamma^l_{ph}(\omega)$ given by Eq. (33) normalized by the cyclotron transition frequency at resonance ω_c^0 for the different photon modes l, as a function of the normalized frequency ω/ω_c^0. $\omega_<$ and $\omega_>$ represent the lower and the upper band edges, respectively. The inset represents the bottom part of the figure, magnified over the frequency range $\omega/\omega_c^0 = 0.8$–1.1. The yellow curve corresponds to l_2 (lowest damping), the red one to l_4, the green one to l_3, and the blue one to l_1 (highest damping).

where $\mathrm{R}(\omega-\omega_0)$ is the rectangular function of width Δ and centered at ω_0. The band-gap parameters $\Delta \approx 180$ GHz and $\omega_0 \approx 496$ GHz represent, respectively, the size and the center frequency of the PBG, and are extracted from the band structure in Fig. 2. Outside the PBG, the damping rate is constant and its value Γ_{ph} can be inferred phenomenologically to reproduce the typical broadening of the modes in THz metallic cavities. τ_l represents the lifetime of the photonic mode l inside the PBG, related to its quality factor by $Q_l = \frac{\omega_l \tau_l}{2}$. The quality factors $Q_{l_1} \approx 1000$, $Q_{l_2} \approx 2100$, $Q_{l_3} \approx 1350$, and $Q_{l_4} \approx 1800$ are calculated by FDTD. The photon damping rates (33) normalized by the cyclotron transition frequency at resonance ω_c^0 are represented in Fig. 11. Finally, following the procedure given in Refs. [40,66] and detailed in Appendix C, we show that the spectrum of the emitted radiation can be put on the form

$$S(\omega) = 16\pi^2 \sum_l \mathrm{Re}\Gamma^l_{ph}(\omega) \int_{-\infty}^{+\infty} d\omega' \times \Big(\sum_{l'} |\underline{\mathcal{V}}_{l,l'}(\omega,\omega')|^2 \mathrm{Re}\Gamma^{l'}_{ph}(-\omega') + |\hat{x}_l(\omega,\omega')|^2 \mathrm{Re}\Gamma_{ex}(-\omega') \Big). \quad (34)$$

The normalized spectrum $S(\omega)\omega_c^0$ given by Eq. (34) is represented in Figs. 12 and 13 (thin blue curves) for different values of the MX damping rate $\Gamma_{ex} = 0.05\omega_c^0$ (lifetime $\tau_{ex} = \frac{1}{\Gamma_{ex}\omega_c^0} \approx 6$ ps) and $\Gamma_{ex} = 0.5\omega_c^0$ ($\tau_{ex} \approx 0.6$ ps), respectively. The thick black curve represents the spectrum (34) with a constant photon damping rate $\mathrm{Re}\Gamma^l_{ph}(\omega) = \Gamma_{ph} = 0.05\omega_c^0$ (Markov approximation), representing the typical photon damping in a metallic cavity with $Q_{ph} \sim 10$. This will be referred to as the

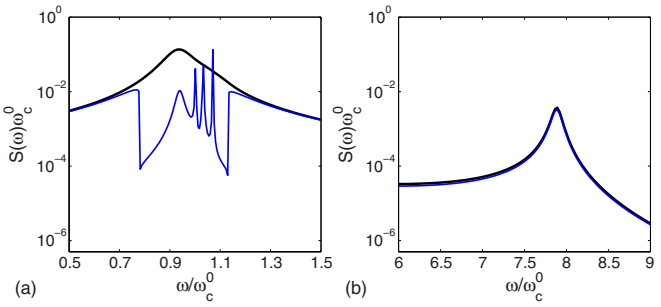

FIG. 12. Normalized spectrum of emitted Casimir photons $S(\omega)\omega_c^0$ calculated numerically from Eq. (34) as a function of the normalized frequency ω/ω_c^0. (a) Corresponds to the frequency range $\omega/\omega_c^0 = 0.5$–1.5, and (b) to the range $\omega/\omega_c^0 = 6$–9. The thin blue curve represents the spectrum emitted out of our PBG-MQW structure, i.e., using the frequency-dependent photon damping rate given by Eq. (33). The thick black curve represents the spectrum calculated in the Markov approximation (cavity case), considering a constant photon damping rate $\mathrm{Re}\Gamma_{ph}(\omega) = 0.05\omega_c^0$. In both cases, the MX damping rate is $\Gamma_{ex} = 0.05\omega_c^0$. Parameters are $\Delta t = 50$ fs, $B_i = 8.86$ T, and $\omega_p/(2\pi) = 20$ THz.

cavity case. Figures 12(a) and 13(a) correspond to the spectra in the PBG frequency range $\omega/\omega_c^0 = 0.5$–1.5. In the cavity case, this part of the spectrum consists of a single peak centered at $\omega \approx \omega_{l_1}$, which becomes broader as the MX damping rate Γ_{ex} is increased. In the case of the photonic crystal structure with photon damping rates given by Eq. (33), the same part of the spectrum consists of narrow peaks which amplitudes roughly decrease by a factor of 10 as Γ_{ex} is increased from $0.05\omega_c^0$ to $0.5\omega_c^0$. However, the linewidths do not depend on the MX damping rate. We also see that the lowest frequency peak on Fig. 12(a) is not present for the largest MX damping rate [Fig. 13(a)].

In Fig. 14, we have magnified two parts of the polariton dispersion plotted on Fig. 6. When the electromagnetic pulse vanishes, the system goes back toward the equilibrium ground state $|G\rangle_i$ by emitting photon pairs with frequencies coincident with the polariton ones ω_λ in the equilibrium state with magnetic field $B_i = 8.86$ T. The emission spectrum is thus peaked at $\omega_\lambda(B_i)$ with $\lambda = 1,2,\ldots,5$, up to the small Lamb shifts induced by the coupling to the reservoirs. From Figs. 7(a) and 8(a), we can see that while the MP2 (MP1 and MP3 have similar properties) has a very small MX

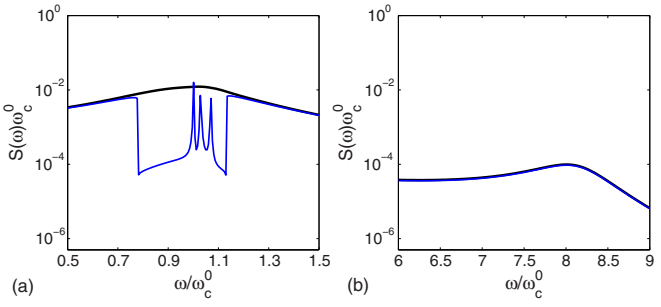

FIG. 13. Same quantities and parameters as in Fig. 12, with a larger MX damping rate $\Gamma_{ex} = 0.5\omega_c^0$.

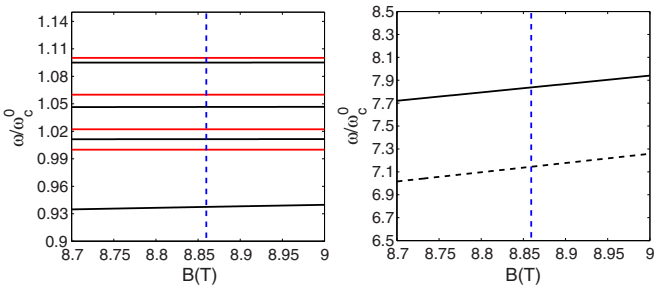

FIG. 14. The polariton dispersion plotted on Fig. 6 is represented in two different frequency ranges. The black solid curves correspond to the polariton frequencies normalized by ω_c^0. The red horizontal solid lines represent the normalized photon mode frequencies ω_l/ω_c^0, and the black dashed line is the normalized cyclotron transition frequency $\omega_c(B)/\omega_c^0$ increasing linearly with the magnetic field. The blue vertical dashed lines correspond to the equilibrium magnetic field $B_i = 8.86$ T.

weight ($|X_{\mathrm{MP2}}|^2 \sim 0.01$), the LP has a large MX weight ($|X_{\mathrm{LP}}|^2 \sim 0.4$) at $B = 8.86$ T and is thus more sensitive to MX damping. This explains why the lowest frequency peak corresponding to the LP vanishes as the MX damping rate is increased.

Figures 12(b) and 13(b) correspond to the normalized spectra $S(\omega)\omega_c^0$ in the frequency range $\omega/\omega_c^0 = 6$–9. The broad peak centered at $\omega/\omega_c^0 \approx 7.9$ corresponds to the UP, and as we can see from Fig. 9(a), its MX weight is large ($|X_{\mathrm{UP}}|^2 \sim 0.8$) at $B = 8.86$ T. This is why the highest frequency peak corresponding to the UP also vanishes as Γ_{ex} is increased. As expected, the cavity and the photonic crystal spectra coincide outside the PBG. We point out that unlike the cavity case where the emitted photon spectrum is very sensitive to MX damping, and becomes almost flat for $\Gamma_{ex} = 0.5\omega_c^0$, the spectrum emitted out of our PBG structure exhibits sharp peaks with well-defined frequencies, which characteristics are extremely robust to the MX broadening expected to increase strongly with temperature and sample disorder. Considering a typical pulse repetition rate of $f_{\mathrm{rep}} = 1$ kHz, the total number of photons emitted per second by the PBG-MQW structure is

$$N_{ph} = f_{\mathrm{rep}} \int d\omega\, S(\omega). \tag{35}$$

Integrating in the frequency range corresponding to the PBG $\omega/\omega_c^0 = 0.5$–1.5, we obtain $N_{ph} \approx 6.5$ and $N_{ph} \approx 5$ for $\Gamma_{ex} = 0.05\omega_c^0$ and $\Gamma_{ex} = 0.5\omega_c^0$, respectively. Despite the very large coupling ratio $\Omega_l/\omega_c \sim 0.8$ achieved here, only a negligible fraction of the energy carried by the pulse is actually converted into Casimir photons. Since the part of the spectrum we are interested in is peaked at frequencies coinciding with the 2D guided modes, the corresponding photon flux is emitted parallel to the QW plane. We point out that the possibility of detecting coherent wave packets at terahertz frequencies containing less than 0.001 photons on average has been demonstrated recently in the context of electro-optical sampling of vacuum fluctuations in free space [68]. A terahertz electric pulse propagating through an electro-optic crystal yields a change of the refractive index which can be probed using ultrashort optical pulses with variable delay time coupled to a differential photocurrent detector. Since the photon detection limit reached in this experiment is about five times smaller than the average number of photon N_{ph}/f_{rep} emitted per pulse out of our PBG structure, the Casimir radiation expected in our proposal should be measurable using ultrabroadband electro-optic sampling. In the context of intersubband excitations coupled to a TM-polarized cavity mode [26,41], a Casimir radiation is expected to occur when switching on the ultrastrong light-matter interaction by using a resonant laser pulse. In this case, the predicted number of emitted photons is comparable to what we predict in the cavity situation [40], e.g., $N_{ph} \approx 28$ and $N_{ph} \approx 9$ for $\Gamma_{ex} = 0.05\omega_c^0$ and $\Gamma_{ex} = 0.5\omega_c^0$, respectively. Despite a photon number $\sim$1 order of magnitude larger than in our proposal, the absence of PBG will make the emission spectra much broader (cf. cavity case in Figs. 12 and 13), and thus more challenging to measure experimentally. In addition, the presence of the Fermi sea in the conduction band with the possibility of creating low-energy excitations is likely to yield an efficient Casimir photon absorption that can not be overcome.

V. CONCLUSION

In conclusion, we propose a system which could allow observation of the all-optical dynamical Casimir effect in realistic experimental conditions. This is achieved thanks to the ultrastrong light-matter coupling between the cyclotron transition of a two-dimensional electron gas sandwiched between 3D PBG material and subjected to a static magnetic field. When a short, intense electromagnetic transient is applied to the structure, the cyclotron transition can be suddenly tuned on resonance with the desired photon guided mode, switching on the light-matter interaction and leading to a Casimir radiation, whose spectrum consists of sharp peaks with frequencies lying in the 3D PBG. We have shown that the characteristics of the radiation spectrum are very robust to the magnetoexciton damping which can be large in realistic experimental conditions. Furthermore, the absence of continuum with associated low-energy excitations can prevent the absorption of the small flux of Casimir photons.

ACKNOWLEDGMENT

The author would like to thank S. John and Y. Laplace for helpful comments.

APPENDIX A: LIGHT-MATTER HAMILTONIAN

In order to calculate the matrix elements entering the linear coupling Hamiltonian (11), it is convenient to introduce the ladder operators d and $d^\dagger$ related to the gauge-invariant momentum $\boldsymbol{\pi}$ by

$$d = \frac{l_c}{\hbar\sqrt{2}}(\pi^y + i\pi^x), \qquad d^\dagger = \frac{l_c}{\hbar\sqrt{2}}(\pi^y - i\pi^x). \tag{A1}$$

These operators act on LL basis states as $d\,|n,k\rangle = \sqrt{n}\,|n-1,k\rangle$ and $d^\dagger\,|n,k\rangle = \sqrt{n+1}\,|n+1,k\rangle$, where $\langle x,y|n,k\rangle = \frac{1}{\sqrt{L}}\chi_{n,k}(x)e^{-iky}$ with $\chi_{n,k}(x)$ given by Eq. (3). Inserting Eqs. (2) and (5) into Eq. (11), the Hamiltonian can

be written as

$$H_I = \sum_l \sum_{n,k} \sum_{n',k'} c^\dagger_{n,k} c_{n',k'} \sqrt{\frac{\hbar}{2\epsilon_0 \epsilon \omega_l a^3}} \left(\frac{e\hbar}{m^* l_c \sqrt{2}}\right) \times \int_{\delta \mathbf{r}_0} d\mathbf{r}\, \xi^*(z) \langle n,k|x,y\rangle d(a_l \tilde{v}_l(\mathbf{r}) + a_l^\dagger \tilde{u}_l^*(\mathbf{r})) \times \xi(z) \langle x,y|n',k'\rangle + \text{H.c}, \quad \text{(A2)}$$

where $\tilde{u}_l(\mathbf{r}) = u_l^y(\mathbf{r}) + i u_l^x(\mathbf{r})$, and $\tilde{v}_l(\mathbf{r}) = u_l^y(\mathbf{r}) - i u_l^x(\mathbf{r})$. Since the mode functions $\mathbf{u}_l(\mathbf{r})$ vary slowly over the volume $\delta\mathbf{r}_0$, we can use the dipole approximation consisting of factorizing the functions $\tilde{u}_l(\mathbf{r})$ and $\tilde{v}_l(\mathbf{r})$ out of the integral, after replacing them by their values at point $\mathbf{r}_0$ (Fig. 5). Moreover, the FDTD calculation shows that the x component $u_l^x(\mathbf{r}_0)$ at point $\mathbf{r}_0$ is negligible for all l, and thus $\widetilde{u}_l(\mathbf{r}_0) \approx u_l^y(\mathbf{r}_0) = \widetilde{v}_l(\mathbf{r}_0)$ where $\widetilde{u}_l(\mathbf{r}_0)$ is a real number. Since the wave functions $\xi(z)$ are normalized in each QW [see Eq. (2)], the z-dependent contribution reduces to unity, and the matrix elements in Eq. (A2) reduce to straightforward evaluations of the kind $\langle n,k|n' \pm 1,k'\rangle$. This scalar product gives the harmonic oscillator selection rule $\delta_{n,n'\pm 1}\delta_{k,k'}$. With these considerations, the linear coupling Hamiltonian can be put on the form

$$H_I = \sum_l \sum_{n,k} \sqrt{\frac{(n+1)\hbar}{2\epsilon_0 \epsilon \omega_l a^3}} \left(\frac{e\hbar}{m^* l_c \sqrt{2}}\right) \times (c^\dagger_{n,k} c_{n+1,k} + c^\dagger_{n+1,k} c_{n,k})(a_l + a_l^\dagger)\tilde{u}_l(\mathbf{r}_0). \quad \text{(A3)}$$

Assuming that the length over which the fermion fields (2) satisfy periodic boundary conditions is given by the lattice constant a, i.e., $N_\phi = a^2/(2\pi l_c)$, and restricting the sum over n to the last fully occupied LL $n = \nu - 1$ (the Pauli principle implies that $\nu - 1 \to \nu$ is the only optically active transition), we finally obtain the Hamiltonian given by Eq. (12).

The $\mathbf{A}^2_{em}$-term Hamiltonian (18) is derived in a similar fashion: We neglect the variations of the slowly varying photonic modes $\mathbf{u}_l(\mathbf{r})$ over the volume $\delta\mathbf{r}_0$. This amounts to factorize this contribution out of the z integral, after replacing it by its value at point $\mathbf{r}_0$. The z integral is then reduced to unity thanks to the normalization of the conduction band wave functions $\xi(z)$, and the matrix elements are proportional to evaluations of the kind $\langle n,k|n',k'\rangle = \delta_{n,n'}\delta_{k,k'}$. Then, we replace the fermion pair operators in Eq. (17) by their mean field values $\langle F| c^\dagger_{n,k} c_{n,k} |F\rangle = \Theta(\nu - 1 - n)$ (Θ is the Heaviside function), and the $\mathbf{A}^2_{em}$ term is found to be proportional to the total number of electrons $n_{qw}\nu N_\phi = n_{qw}\rho a^2$.

APPENDIX B: DIAGONALIZATION PROCEDURE

In this Appendix, we introduce the matrix formalism which helps us calculating the polariton frequencies ω_λ. The eigenvalue problem $[p_\lambda, H_{\text{pol}}] = \hbar\omega_\lambda p_\lambda$ can be put in the matrix form (underlines stand for matrices and hats for row or column vectors)

$$\underline{\mathcal{M}}\hat{\varphi}_\lambda = \omega_\lambda \hat{\varphi}_\lambda, \quad \text{(B1)}$$

where the so-called Hopfield matrix [46,64] reads as

$$\underline{\mathcal{M}} = \begin{pmatrix} \underline{\omega} + 2\underline{D} & \hat{\Omega} & 2\underline{D} & \hat{\Omega} \\ \hat{\Omega}^T & \omega_c & \hat{\Omega}^T & 0 \\ -2\underline{D} & -\hat{\Omega} & -\underline{\omega} - 2\underline{D} & -\hat{\Omega} \\ -\hat{\Omega}^T & 0 & -\hat{\Omega}^T & -\omega_c \end{pmatrix}, \quad \text{(B2)}$$

and the eigenvectors (the symbol T denotes the transpose operation)

$$\hat{\varphi}_\lambda = \left(W_{l_1,\lambda} \ldots W_{l_4,\lambda}\ X_\lambda\ Y_{l_1,\lambda} \ldots Y_{l_4,\lambda}\ Z_\lambda\right)^T. \quad \text{(B3)}$$

$\underline{\omega}$ denotes the 4×4 diagonal matrix with the photon mode frequencies ω_l along the diagonal. $\hat{\Omega} = (\Omega_{l_1}\ \Omega_{l_1}\ \Omega_{l_3}\ \Omega_{l_4})^T$ is the column vector involving the vacuum Rabi frequencies for each mode l, and $\underline{D}$ is the 4×4 matrix with elements $D_{l,l'}$. The polariton frequencies ω_λ and eigenvectors $\hat{\varphi}_\lambda$ can be found by diagonalizing the 10×10 matrix $\underline{\mathcal{M}}$ numerically.

APPENDIX C: EMISSION SPECTRUM

Here, we calculate the spectrum of the emitted radiation in the framework of the input-output formalism. Such a calculation has already been performed in the case of a single photonic mode [66], as well as considering a periodic modulation of the VRF [40] (parametric oscillation). We generalize this formalism to the case of many photon modes coupled to statistically independent reservoirs, and for a general time modulation of the Hamiltonian parameters. Let us start by writing the equations of motion for the reservoir operators in the Heisenberg picture:

$$\frac{da_{\eta_l}(t)}{dt} = -\frac{i}{\hbar}[a_{\eta_l}, H](t) = -i\omega_{\eta_l} a_{\eta_l}(t) - i\kappa^*_{\eta_l} a_l(t),$$
$$\frac{db_\mu(t)}{dt} = -\frac{i}{\hbar}[b_\mu, H](t) = -i\omega_\mu b_\mu(t) - i\kappa^*_\mu b(t), \quad \text{(C1)}$$

which can be solved formally as

$$a_{\eta_l}(t) = e^{-i\omega_{\eta_l}(t-t_0)} a_{\eta_l}(t_0) - i\kappa^*_{\eta_l} \int_{t_0}^t dt' e^{-i\omega_{\eta_l}(t-t')} a_l(t'),$$
$$b_\mu(t) = e^{-i\omega_\mu(t-t_0)} b_\mu(t_0) - i\kappa^*_\mu \int_{t_0}^t dt' e^{-i\omega_\mu(t-t')} b(t'). \quad \text{(C2)}$$

We inject the solutions (C2) into the equations of motion for the photon modes a_l and the MX operator b. When the time scales of the system and the environment are well separated, we can take the limits $t_0 \to -\infty$ and $t \to +\infty$, and the equations of motion can be written as

$$\frac{da_l(t)}{dt} = -\frac{i}{\hbar}[a_l, H_{\text{pol}}](t) - F^l_{ph}(t) - \int dt' \Gamma^l_{ph}(t-t') a_l(t'),$$
$$\frac{db(t)}{dt} = -\frac{i}{\hbar}[b, H_{\text{pol}}](t) - F_{el}(t) - \int dt' \Gamma_{ex}(t-t') b(t'). \quad \text{(C3)}$$

The damping memory kernels are defined as [$\Theta(t)$ is the Heaviside function]

$$\Gamma^l_{ph}(t) = \Theta(t) \sum_{\eta_l} |\kappa_{\eta_l}|^2 e^{-i\omega_{\eta_l} t},$$
$$\Gamma_{ex}(t) = \Theta(t) \sum_{\mu} |\kappa_\mu|^2 e^{-i\omega_\mu t}, \quad \text{(C4)}$$

with the associated Fourier transforms $\Gamma^l_{ph}(\omega) = \int dt\, e^{i\omega t}\Gamma^l_{ph}(t)$ and $\Gamma_{ex}(\omega) = \int dt\, e^{i\omega t}\Gamma_{ex}(t)$. We have also introduced the fluctuating Langevin forces

$$F^l_{ph}(t) = i\sum_{\eta_l}\kappa_{\eta_l}e^{-i\omega_{\eta_l}t}a^{\rm in}_{\eta_l},$$
$$F_{ex}(t) = i\sum_{\mu}\kappa_{\mu}e^{-i\omega_{\mu}t}b^{\rm in}_{\mu}, \tag{C5}$$

involving the input annihilation operators $a^{\rm in}_{\eta_l} = \lim_{t\to-\infty} a_{\eta_l}(t)e^{i\omega_{\eta_l}t}$ and $b^{\rm in}_{\mu} = \lim_{t\to-\infty} b_{\mu}(t)e^{i\omega_{\mu}t}$. The latter destroys an excitation in the associated reservoir before the perturbation is turned on. The system (C3) forms a closed set of equations and can be solved conveniently in the Fourier space using matrix notations as

$$\hat{v}(\omega) = 2i\pi\int d\omega'\underline{\mathcal{T}}^{-1}(\omega,\omega')\hat{F}(\omega'). \tag{C6}$$

The two column vectors $\hat{v}(\omega)$ and $\hat{F}(\omega)$ are defined as

$$\hat{v}(\omega) = (a_{l_1}(\omega)\dots a_{l_4}(\omega)\; b(\omega)\; a^\dagger_{l_1}(-\omega)\dots a^\dagger_{l_4}(-\omega)\; b^\dagger(-\omega))^T,$$
$$\hat{F}(\omega) = \big(F^{l_1}_{ph}(\omega)\dots F^{l_4}_{ph}(\omega)\; F_{ex}(\omega) \times F^{l_1\dagger}_{ph}(-\omega)\dots F^{l_4\dagger}_{ph}(-\omega)\; F^\dagger_{ex}(-\omega)\big)^T, \tag{C7}$$

and involve the Fourier transforms of the MXs and photon operators

$$a_l(\omega) = \int dt\, e^{i\omega t}a_l(t), \qquad b(\omega) = \int dt\, e^{i\omega t}b(t), \tag{C8}$$

as well as the Fourier transforms of the Langevin forces

$$F^l_{ph}(\omega) = 2i\pi\sum_{\eta_l}\kappa_{\eta_l}\delta(\omega-\omega_{\eta_l})a^{\rm in}_{\eta_l},$$
$$F_{ex}(\omega) = 2i\pi\sum_{\mu}\kappa_{\mu}\delta(\omega-\omega_{\mu})b^{\rm in}_{\mu}. \tag{C9}$$

$\underline{\mathcal{T}}^{-1}(\omega,\omega')$ represents the inverse of the matrix $\underline{\mathcal{T}}(\omega,\omega')$ defined as

$$\underline{\mathcal{T}}(\omega,\omega') = 2\pi[\underline{\mathcal{M}}_i - \omega\underline{\mathbb{I}} - i\underline{\Gamma}(\omega)]\delta(\omega-\omega') + \underline{\Delta\mathcal{M}}(\omega-\omega'), \tag{C10}$$

and related to the matrix $\underline{\mathcal{T}}^{-1}$ by the relation

$$\int d\omega''\underline{\mathcal{T}}^{-1}(\omega,\omega'')\underline{\mathcal{T}}(\omega'',\omega') = \underline{\mathbb{I}}\otimes\delta(\omega-\omega'). \tag{C11}$$

$\underline{\mathbb{I}}$ denotes the 10×10 identity matrix, $\underline{\mathcal{M}}_i$ is the matrix defined in Eq. (B2), where the quantities depending on the magnetic field ($\hat{\Omega}$ and ω_c) are evaluated at $B = B_i$. The matrix taking the damping rates/Lamb shifts into account reads as

$$\underline{\Gamma}(\omega) = \begin{pmatrix} \underline{\Gamma}_{ph}(\omega) & \hat{0} & \underline{0} & \hat{0} \\ \hat{0}^T & \Gamma_{ex}(\omega) & \hat{0}^T & 0 \\ \underline{0} & \hat{0} & \underline{\Gamma}^*_{ph}(-\omega) & \hat{0} \\ \hat{0}^T & 0 & \hat{0}^T & \Gamma^*_{ex}(-\omega) \end{pmatrix}, \tag{C12}$$

and the time-modulation matrix is

$$\underline{\Delta\mathcal{M}}(\omega) = \begin{pmatrix} \underline{0} & \Delta\hat{\Omega}(\omega) & \underline{0} & \Delta\hat{\Omega}(\omega) \\ \Delta\hat{\Omega}^T(\omega) & \Delta\omega_c(\omega) & \Delta\hat{\Omega}^T(\omega) & 0 \\ \underline{0} & -\Delta\hat{\Omega}(\omega) & \underline{0} & -\Delta\hat{\Omega}(\omega) \\ -\Delta\hat{\Omega}^T(\omega) & 0 & -\Delta\hat{\Omega}^T(\omega) & -\Delta\omega_c(\omega) \end{pmatrix}. \tag{C13}$$

$\underline{\Gamma}_{ph}(\omega)$ corresponds to the 4×4 diagonal matrix with the complex numbers $\Gamma^l_{ph}(\omega)$ for each mode l along the diagonal, $\underline{0}$ to the 4×4 null matrix, and $\hat{0}$ to the null column vector $(0\;0\;0\;0)^T$. The symbol * stands for the complex conjugate operation. Finally, $\Delta\omega_c(\omega)$ represents the Fourier transform of the time-dependent part of the cyclotron transition frequency $\Delta\omega_c(t)$, and $\Delta\hat{\Omega}(\omega) = [\Delta\Omega_{l_1}(\omega)\;\Delta\Omega_{l_2}(\omega)\;\Delta\Omega_{l_3}(\omega)\;\Delta\Omega_{l_4}(\omega)]^T$ is the column vector involving the Fourier transform of the time-dependent part of the VRF $\Delta\Omega_l(t)$ for each mode l. $\Delta\omega_c(t)$ and $\Delta\Omega_l(t)$ are defined in Eq. (25). Let us introduce the output annihilation operators which destroy an excitation in the associated reservoir after the perturbation is turned off:

$$a^{\rm out}_{\eta_l} = \lim_{t\to+\infty} a_{\eta_l}(t)e^{i\omega_{\eta_l}t}, \qquad b^{\rm out}_{\mu} = \lim_{t\to+\infty} b_{\mu}(t)e^{i\omega_{\mu}t}. \tag{C14}$$

We can use Eqs. (C2) to find a linear relationship between input and output operators:

$$a^{\rm out}_{\eta_l} = a^{\rm in}_{\eta_l} - i\kappa^*_{\eta_l}a_l(\omega_{\eta_l}), \qquad b^{\rm out}_{\mu} = b^{\rm in}_{\mu} - i\kappa^*_{\mu}b(\omega_{\mu}), \tag{C15}$$

which allows to calculate the spectrum $S(\omega)$ of the emitted radiation. This spectrum, observed a long time after the perturbation is turned off, is indeed proportional to the sum of the photonic populations over the different reservoirs η_l:

$$S(\omega) = \sum_l\sum_{\eta_l}\delta(\omega-\omega_{\eta_l})\langle a^{\rm out\dagger}_{\eta_l}a^{\rm out}_{\eta_l}\rangle_R. \tag{C16}$$

The notation $\langle\dots\rangle_R$ denotes the expectation value on a given reservoir. We now use Eq. (C15) to express the expectation value $\langle a^{\rm out\dagger}_{\eta_l}a^{\rm out}_{\eta_l}\rangle_R$ as

$$\langle a^{\rm out\dagger}_{\eta_l}a^{\rm out}_{\eta_l}\rangle_R = \langle a^{\rm in\dagger}_{\eta_l}a^{\rm in}_{\eta_l}\rangle_R + |\kappa_{\eta_l}|^2\langle a^\dagger_l(\omega_{\eta_l})a_l(\omega_{\eta_l})\rangle_R. \tag{C17}$$

From Eqs. (C5) and (C6), we obtain a linear relationship between the photon mode operators $a^{(\dagger)}_l$ and the input operators $a^{\rm in(\dagger)}_{\eta_l}$ and $b^{\rm in(\dagger)}_{\mu}$ associated with the different reservoirs. Before the perturbation is turned on, the reservoirs are in their ground state (vacuum) and, hence, $\langle a^{\rm in\dagger}_{\eta_l}a^{\rm in}_{\eta_l}\rangle_R = 0\;\forall\;\eta_l$, $\langle b^{\rm in\dagger}_{\mu}b^{\rm in}_{\mu}\rangle_R = 0\;\forall\;\mu$. The only nonvanishing correlation functions for the Langevin forces are $\langle F^l_{ph}(-\omega)F^{l'\dagger}_{ph}(-\omega')\rangle_R$ and $\langle F_{ex}(-\omega)F^\dagger_{ex}(-\omega')\rangle_R$. Let us introduce the formal

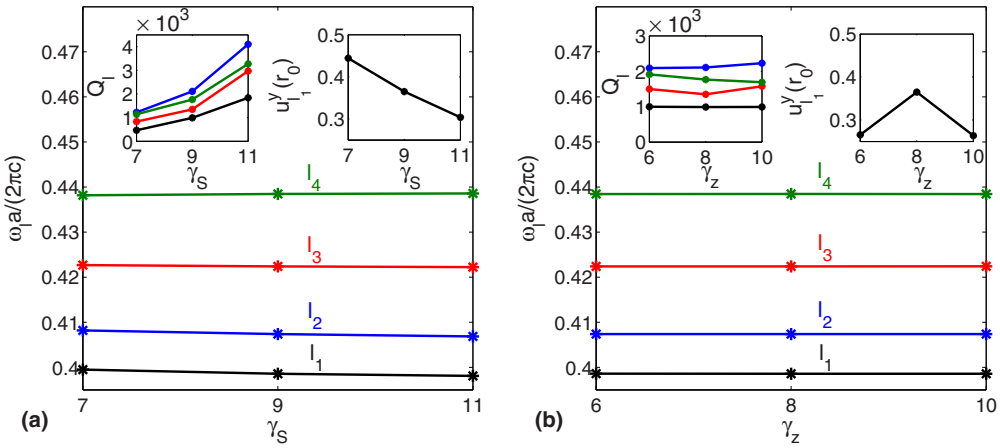

FIG. 15. (a) Normalized mode frequencies $\frac{\omega_l a}{2\pi c}$ as a function of the number of woodpile periods in the x and y directions γ_S. Left inset: quality factor Q_l as a function of γ_S. Right inset: y component of the mode function $u^y_{l_1}$ evaluated at point $\mathbf{r}_0$, as a function of γ_S. The other parameters are $\gamma_z = 8$, $t_{sp} = 500a/c$, and $res = 32$. (b) Same quantities represented as a function of the number of woodpile periods in the z direction γ_z. Parameters: $\gamma_S = 9$, $t_{sp} = 500a/c$, and $res = 32$.

notations

$$\underline{\mathcal{T}}^{-1}(\omega,\omega') = \begin{pmatrix} \underline{\mathcal{U}}(\omega,\omega') & \hat{w}(\omega,\omega') & \underline{\mathcal{V}}(\omega,\omega') & \hat{x}(\omega,\omega') \\ \hat{y}(\omega,\omega') & f(\omega,\omega') & \hat{z}(\omega,\omega') & g(\omega,\omega') \\ -\underline{\mathcal{V}}^*(-\omega,-\omega') & -\hat{x}^*(-\omega,-\omega') & -\underline{\mathcal{U}}^*(-\omega,-\omega') & -\hat{w}^*(-\omega,-\omega') \\ -\hat{z}^*(-\omega,-\omega') & -g^*(-\omega,-\omega') & -\hat{y}^*(-\omega,-\omega') & -f^*(-\omega,-\omega') \end{pmatrix}, \tag{C18}$$

where $\underline{\mathcal{U}}$ and $\underline{\mathcal{V}}$ denote 4×4 matrices, $\hat{w}$ and $\hat{x}$ are column vectors, $\hat{y}$ and $\hat{z}$ are row vectors, and f, g are complex numbers. Using Eqs. (C6) and (C18), we obtain

$$\langle a_l^\dagger(\omega) a_l(\omega)\rangle_R = 16\pi^3 \int_{-\infty}^{+\infty} d\omega' \times \left(\sum_{l'} |\underline{\mathcal{V}}_{l,l'}(\omega,\omega')|^2 \mathrm{Re}\Gamma^{l'}_{ph}(-\omega') + |\hat{x}_l(\omega,\omega')|^2 \mathrm{Re}\Gamma_{ex}(-\omega') \right), \tag{C19}$$

and inserting (C19) back into (C17), the emitted photon spectrum (C16) takes the form

$$S(\omega) = 16\pi^2 \sum_l \mathrm{Re}\Gamma^l_{ph}(-\omega') \int_{-\infty}^{+\infty} d\omega' \times \left(\sum_{l'} |\underline{\mathcal{V}}_{l,l'}(\omega,\omega')|^2 \mathrm{Re}\Gamma^{l'}_{ph}(-\omega') + |\hat{x}_l(\omega,\omega')|^2 \mathrm{Re}\Gamma_{ex}(-\omega') \right). \tag{C20}$$

Finally, the quantities $\underline{\mathcal{V}}_{l,l'}(\omega,\omega')$ and $\hat{x}_l(\omega,\omega')$ are calculated by inverting the matrix $\underline{\mathcal{T}}^{-1}$ numerically.

APPENDIX D: FINITE-DIFFERENCE TIME-DOMAIN CALCULATIONS

In this Appendix, we describe the numerical methods used to find the electromagnetic modes and the LDOS of the finite PBG-MQW structure. The effects of changing the simulation parameters on the mode frequencies, quality factors, and spatial distribution are discussed. We have performed time-domain electromagnetic simulations using the MEEP software, running on a 32-core distributed-memory parallel machine with standard MPI. The finite dielectric structure is described in Sec. II B 2, and consists of γ_S periods of woodpile material in the x and y directions, and γ_z periods in the z direction. A defect layer with relative permittivity $\epsilon_d = 13$ and thickness $h_d = 0.04a$ lies in the middle of the woodpile structure. The relative permittivity of the germanium logs is $\epsilon = 16$. The structure is surrounded by an air padding layer and then by an absorbing layer (perfectly matched layers), each one having a thickness a. The values of ω_l and $\mathbf{u}_l(\mathbf{r}_0)$ used in Secs. III and IV are obtained using a computational grid resolution of $res = 32$ pixels per distance unit a, which means that the defect layer corresponds to ≈ 1.3 pixel. In this case, the dielectric structure has $\gamma_S = 9$ woodpile periods in the xy plane and $\gamma_z = 8$ in the z direction. The point-dipole current source is randomly positioned, aligned in the y direction, and consists of a Gaussian envelope of width df, modulated by a sinusoidal current with frequency f. After the sources are finished, some signal processing on the fields is performed by the HARMINV function during an additional period of time $t_{sp} = 500a/c$. By tuning f and df, we can determine the mode frequencies ω_l and the quality factors Q_l. Then, we output field snapshots over a whole period for each mode l, normalize the fields according to Eq. (6), and identify the temporal amplitude $\mathbf{u}_l$ at position $\mathbf{r}_0$. We use Eq. (13) to calculate the VRFs Ω_l. The estimated error in the frequencies due to the signal processing is $< 10^{-6} \times \frac{2\pi c}{a}$.

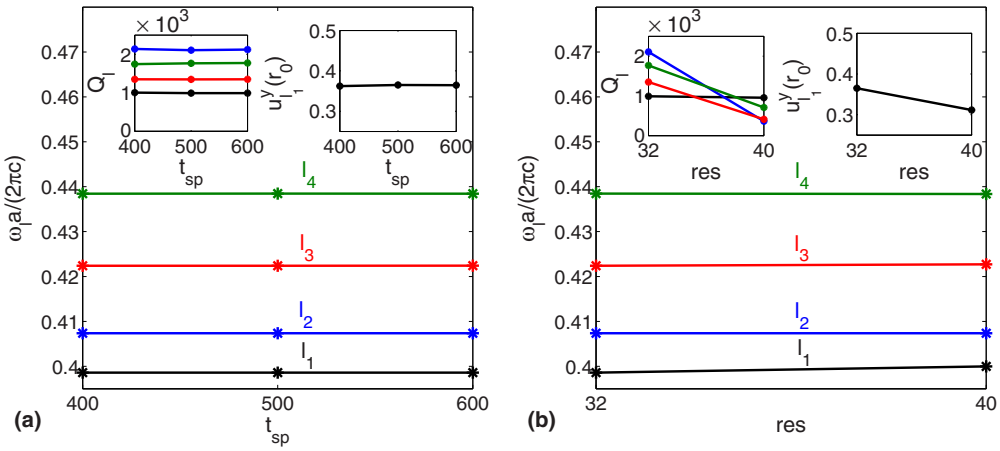

FIG. 16. (a) Normalized mode frequencies $\frac{\omega_l a}{2\pi c}$ as a function of the signal-processing time t_{sp}. Left inset: quality factor Q_l as a function of t_{sp}. Right inset: y component of the mode function $u^y_{l_1}$ evaluated at point $\mathbf{r}_0$, as a function of t_{sp}. The other parameters are $\gamma_S = 9$, $\gamma_z = 8$, and $res = 32$. (b) Same quantities represented as a function of the computational grid resolution res, with parameters $\gamma_S = 9$, $\gamma_z = 8$, and $t_{sp} = 500a/c$.

The normalized mode frequencies $\frac{\omega_l a}{2\pi c}$, quality factors Q_l, and amplitudes $u^y_{l_1}(\mathbf{r}_0)$ are represented on Figs. 15 and 16, as a function of γ_S, γ_z, t_{sp}, and res. Each plot corresponds to a single-parameter change while the others are kept equal to their reference values $\gamma_S = 9$, $\gamma_z = 8$, $t_{sp} = 500a/c$, $res = 32$ used in Secs. III and IV. The computational time for a single run (HARMINV processing+fields output) ranges from 30 h up to more than 40 h for the heaviest calculation. Regarding the signal-processing time, Fig. 16(a) shows that numerical convergence is reached for $t_{sp} = 500a/c$. Overall, the change in the mode frequencies is rather small, and reaches its maximum value ~0.35% for the mode l_1 with $\gamma_S = 9$, $\gamma_z = 8$, $t_{sp} = 500a/c$, and $res = 40$. From Figs. 15(a) and 15(b), we see that while the asymptotic regime for the quality factors is reached in the range $\gamma_z = 6$–10, the latter increase exponentially with γ_S. By increasing the resolution to $res = 40$, we see that the quality factors of the modes l_2, l_3, and l_4 used in Sec. IV C are overestimated by a factor ~2–6 [Fig. 16(b)]. We have checked that decreasing the resolution to $res = 24$ (defect layer less than one pixel) yields a delocalization of the modes over the whole structure as if there was no defect. The change in the amplitude $u^y_{l_1}(\mathbf{r}_0)$ results in a change in the VRF Ω_{l_1}, reaching 28% for $\gamma_S = 9$, $\gamma_z = 10$, $t_{sp} = 500a/c$, and $res = 32$. As a function of the resolution and the signal-processing time, the maximum change in the VRF is 15%, reached for $\gamma_z = 8$, $t_{sp} = 500a/c$, and $res = 40$. The other VRFs Ω_{l_j} for $j = 2,3,4$ exhibit a similar sensitivity to changes in the simulation parameters. Assuming a drop of 28% in the VRFs Ω_l used in Sec. III A, the number of Casimir photons emitted per second is decreased to $N_{ph} \approx 2.2$ and $N_{ph} \approx 1.7$ for $\Gamma_{ex} = 0.05\omega_c^0$ and $\Gamma_{ex} = 0.5\omega_c^0$, respectively, still larger than the detection limit of Ref. [68].

[1] J.-M. Raimond, M. Brune, and S. Haroche, Rev. Mod. Phys. **73**, 565 (2001).
[2] Y. Colombe, T. Steinmetz, G. Dubois, F. Linke, D. Hunger, and J. Reichel, Nature (London) **450**, 272 (2007).
[3] D. Dini, R. Köhler, A. Tredicucci, G. Biasiol, and L. Sorba, Phys. Rev. Lett. **90**, 116401 (2003).
[4] J. P. Reithmaier, G. Sek, A. Löffler, C. Hofmann, S. Kuhn, S. Reitzenstein, L. V. Keldysh, V. D. Kulakovskii, T. L. Reinecke, and A. Forchel, Nature (London) **432**, 197 (2004).
[5] D. I. Schuster *et al.*, Nature (London) **445**, 515 (2007).
[6] R. J. Schoelkopf and S. M. Girvin, Nature (London) **451**, 664 (2008).
[7] H. Deng, H. Haug, and Y. Yamamoto, Rev. Mod. Phys. **82**, 1489 (2010).
[8] I. Carusotto and C. Ciuti, Rev. Mod. Phys. **85**, 299 (2013).
[9] S. John, Phys. Rev. Lett. **58**, 2486 (1987).
[10] E. Yablonovitch, Phys. Rev. Lett. **58**, 2059 (1987).
[11] J. D. Joannopoulos, S. G. Johnson, J. N. Winn, and R. D. Meade, *Photonic Crystals: Molding the Flow of Light*, 2nd ed. (Princeton University Press, Princeton, NJ, 2008).
[12] J. D. Joannopoulos, P. R. Villeuneuve, and S. Fan, Nature (London) **386**, 143 (1997).
[13] S. John and S. Yang, Phys. Rev. Lett. **99**, 046801 (2007).
[14] Y. Akahane, T. Asano, B.-S. Song, and S. Noda, Nature (London) **425**, 944 (2003).
[15] A. Badolato, K. Hennessy, M. Atatüre, J. Dreiser, E. Hu, P. M. Petroff, and A. Imamoglu, Science **308**, 1158 (2005).
[16] L. C. Andreani, D. Gerace, and M. Agio, Phys. Status Solidi B **242**, 2197 (2005).
[17] K. Hennessy, A. Badolato, M. Winger, D. Gerace, M. Atatüre, S. Gulde, S. Fält, E. L. Hu, and A. Imamoglu, Nature (London) **445**, 896 (2007).
[18] D. Gerace and L. C. Andreani, Phys. Rev. B **75**, 235325 (2007).

[19] P. De Maagt, R. Gonzalo, Y. Vardaxoglou, and J.-M. Baracco, IEEE Trans. Antennas Propagat. **51**, 2667 (2003).

[20] C. Yee, N. Jukam, and M. Sherwin, Appl. Phys. Lett. **91**, 194104 (2007).

[21] Z. Wu, A. Young, M. Gehm, and H. Xin, Microw. Opt. Tech. Lett. **52**, 678 (2010).

[22] H. Zhang, L. A. Dunbar, G. Scalari, R. Houdré, and J. Faist, Opt. Express **15**, 16818 (2007).

[23] Y. Chassagneux, R. Colombelli, W. Maineult, S. Barbieri, H. E. Beere, D. A. Ritchie, S. P. Khanna, E. H. Linfield, and A. G. Davies, Nature (London) **457**, 174 (2009).

[24] C. Ciuti, G. Bastard, and I. Carusotto, Phys. Rev. B **72**, 115303 (2005).

[25] A. A. Anappara, S. De Liberato, A. Tredicucci, C. Ciuti, G. Biasiol, L. Sorba, and F. Beltram, Phys. Rev. B **79**, 201303(R) (2009).

[26] G. Gunter *et al.*, Nature (London) **458**, 178 (2009).

[27] Y. Todorov, A. M. Andrews, R. Colombelli, S. De Liberato, C. Ciuti, P. Klang, G. Strasser, and C. Sirtori, Phys. Rev. Lett. **105**, 196402 (2010).

[28] M. Geiser, F. Castellano, G. Scalari, M. Beck, L. Nevou, and J. Faist, Phys. Rev. Lett. **108**, 106402 (2012).

[29] D. Dietze, A. M. Andrews, P. Klang, G. Strasser, K. Unterrainer, and J. Darmo, Appl. Phys. Lett. **103**, 201106 (2013).

[30] I. Carusotto, M. Antezza, F. Bariani, S. De Liberato, and C. Ciuti, Phys. Rev. A **77**, 063621 (2008).

[31] P. W. Milonni, *The Quantum Vacuum: An Introduction to Quantum Electrodynamics* (Academic, San Diego, 1994).

[32] S. A. Fulling and P. C. W. Davis, Proc. R. Soc. London, Ser. A **348**, 396 (1976).

[33] C. M. Wilson, G. Johansson, A. Pourkabirian, M. Simoen, J. R. Johansson, T. Duty, F. Nori, and P. Delsing, Nature (London) **479**, 376 (2011).

[34] E. Yablonovitch, Phys. Rev. Lett. **62**, 1742 (1989).

[35] V. V. Dodonov, A. B. Klimov, and D. E. Nikonov, Phys. Rev. A **47**, 4422 (1993).

[36] F. X. Dezael and A. Lambrecht, Europhys. Lett. **89**, 14001 (2010).

[37] Y. Lozovik, V. Tsvetus, and E. Vinogradov, Pis'ma Zh. Éksp. Teor. Fiz. **61**, 771 (1995) [JETP Lett. **61**, 723 (1995)].

[38] C. Braggio, G. Bressi, G. Carugno, C. Del Noce, G. Galeazzi, A. Lombardi, A. Palmieri, G. Ruoso, and D. Zanello, Europhys. Lett. **70**, 754 (2005).

[39] I. Carusotto, S. De Liberato, D. Gerace, and C. Ciuti, Phys. Rev. A **85**, 023805 (2012).

[40] S. De Liberato, C. Ciuti, and I. Carusotto, Phys. Rev. Lett. **98**, 103602 (2007).

[41] M. Porer, J.-M. Ménard, A. Leitenstorfer, R. Huber, R. Degl'Innocenti, S. Zanotto, G. Biasiol, L. Sorba, and A. Tredicucci, Phys. Rev. B **85**, 081302 (2012).

[42] G. Scalari *et al.*, Science **335**, 1323 (2012).

[43] G. Scalari, C. Maissen, D. Hagenmüller, S. De Liberato, C. Ciuti, C. Reichl, W. Wegscheider, D. Schuh, M. Beck, and J. Faist, J. Appl. Phys. **113**, 136510 (2013).

[44] G. Scalari, C. Maissen, S. Cibella, R. Leoni, P. Carelli, F. Valmorra, M. Beck, and J. Faist, New J. Phys. **16**, 033005 (2014).

[45] C. Maissen, G. Scalari, F. Valmorra, M. Beck, J. Faist, S. Cibella, R. Leoni, C. Reichl, C. Charpentier, and W. Wegscheider, Phys. Rev. B **90**, 205309 (2014).

[46] D. Hagenmuller, S. De Liberato, and C. Ciuti, Phys. Rev. B **81**, 235303 (2010).

[47] A. Sell, A. Leitenstorfer, and R. Huber, Opt. Lett. **33**, 2767 (2008).

[48] T. Kampfrath, K. Tanaka, and K. A. Nelson, Nat. Photonics **7**, 680 (2013).

[49] L. D. Landau and E. M. Lifschitz, *Quantum Mechanics: Non-relativistic Theory. Course of Theoretical Physics*, Vol. 3, 3rd ed. (Pergamon, London, 1977).

[50] D. R. Hofstadter, Phys. Rev. B **14**, 2239 (1976).

[51] K. M. Ho, C. T. Chan, C. M. Soukoulis, R. Biswas, and M. Sigalas, Solid State Commun. **89**, 413 (1994).

[52] R. Gonzalo, B. Martinez, C. M. Mann, H. Pellemans, P. H. Bolivar, and P. De Maagt, IEEE Trans. Microwave Theory Tech. **50**, 2384 (2002).

[53] S. Y. Lin, J. G. Fleming, D. L. Hetherington, B. K. Smith, R. Biswas, K. M. Ho, M. M. Sigalas, W. Zubrzycki, S. R. Kurtz, and J. Bur, Nature (London) **394**, 251 (1998).

[54] S. Noda, K. Tomoda, N. Yamamoto, and A. Chutinan, Science **289**, 604 (2000).

[55] C. McGuinness *et al.*, AIP Conf. Proc. **1086**, 544 (2009).

[56] A. Tandaechanurat, S. Ishida, D. Guimard, M. Nomura, S. Iwamoto, and Y. Arakawa, Nat. Photonics **5**, 91 (2011).

[57] D. Grischkowsky, S. Keiding, M. Van Exter, and C. Fattinger, J. Opt. Soc. Am. B **7**, 2006 (1990).

[58] K. Sakoda, *Optical Properties of Photonic Crystals* (Springer, Berlin, 2005).

[59] H. Westfahl, A. H. Castro Neto, and A. O. Caldeira, Phys. Rev. B **55**, R7347(R) (1997).

[60] G. F. Giuliani and G. Vignale, *Quantum Theory of the Electron Liquid* (Cambridge University Press, Cambridge, 2005).

[61] W. Kohn, Phys. Rev. **123**, 1242 (1961).

[62] T. Ando, A. B. Fowler, and F. Stern, Rev. Mod. Phys. **54**, 437 (1982).

[63] D. Tolkunov and D. Solenov, Phys. Rev. B **75**, 024402 (2007).

[64] J. J. Hopfield, Phys. Rev. **112**, 1555 (1958).

[65] M. O. Scully and M. S. Zubairy, *Quantum Optics* (Cambridge University Press, Cambridge, 1997).

[66] C. Ciuti and I. Carusotto, Phys. Rev. A **74**, 033811 (2006).

[67] N. Vats and S. John, Phys. Rev. A **58**, 4168 (1998).

[68] C. Riek, D. V. Seletskiy, A. S. Moskalenko, J. F. Schmidt, P. Krauspe, S. Eckart, S. Eggert, G. Burkard, and A. Leitenstorfer, Science **350**, 420 (2015).